1 **3D *in situ* imaging of female reproductive tract reveals molecular signatures of fertilizing**
2 **spermatozoa in mice**

3

4 Lukas Ded[1,3], Jae Yeon Hwang[1], Kiyoshi Miki[4], Huanan F. Shi[1], and Jean-Ju Chung[1,2*]

5

6 [1]Department of Cellular & Molecular Physiology, [2]Department of Obstetrics, Gynecology, and
7 Reproductive Sciences, Yale School of Medicine, New Haven, CT, USA. [3]Laboratory of
8 Reproductive Biology, Institute of Biotechnology CAS, v.v.i., BIOCEV, Vestec, Czech Republic.
9 [4]Boston Children's Hospital, Boston, MA, USA.

10

11 *Corresponding author: Jean-Ju Chung (jean-ju.chung@yale.edu)

12

Abstract

14 Out of millions of ejaculated sperm, only a few reach the fertilization site in mammals. Flagellar
15 Ca^{2+} signaling nanodomains, organized by multi-subunit CatSper calcium channel complexes,
16 are pivotal for sperm migration in the female tract, implicating CatSper-dependent mechanisms
17 in sperm selection. Here, using biochemical and pharmacological studies, we demonstrate that
18 CatSper1 is an O-linked glycosylated protein, undergoing capacitation-induced processing
19 dependent on Ca^{2+} and phosphorylation cascades. CatSper1 processing correlates with protein
20 tyrosine phosphorylation (pY) development in sperm cells capacitated *in vitro* and *in vivo*. Using
21 3D *in situ* molecular imaging and ANN-based automatic detection of sperm distributed along the
22 cleared female tract, we demonstrate that all spermatozoa past the UTJ possess intact CatSper1
23 signals. Together, we reveal that fertilizing mouse spermatozoa *in situ* are characterized by intact
24 CatSper channel, lack of pY, and reacted acrosomes. These findings provide molecular insight
25 into sperm selection for successful fertilization in the female reproductive tract.

Introduction

In most mammals, millions or billions of spermatozoa are deposited into the cervix upon coitus. Yet less than 100 spermatozoa are found at the fertilization site, called ampulla, and only 10-12 spermatozoa are observed around an oocyte (Kolle, 2015; Suarez, 2002). This implies the presence of mechanisms to select sperm as they travel through the female reproductive tract and to eliminate non-fertilizing, surplus spermatozoa once the egg is fertilized (Sakkas et al., 2015). Recent *ex vivo* imaging studies combined with mouse genetics have shown that surface molecules on the sperm plasma membranes such as ADAM family proteins are essential for the sperm to pass through the utero-tubal junction (UTJ) (Fujihara et al., 2018). By contrast, whether such selection and elimination within the oviduct requires specific molecular signatures and cellular signaling of spermatozoa is not fully understood.

Mammalian sperm undergo capacitation, a physiological process to obtain the ability to fertilize the egg, naturally inside the oviduct (Austin, 1951; Chang, 1951). The emulation of sperm capacitation *in vitro* led to the development of *in vitro* fertilization (IVF) techniques (Steptoe and Edwards, 1976; Wang and Sauer, 2006). Since then, most studies on sperm capacitation and gamete interaction have been carried out under *in vitro* conditions. However, mounting evidence suggests that *in vitro* sperm capacitation does not precisely reproduce the time- and space-dependent *in vivo* events in the oviduct. Protein tyrosine phosphorylation (pY), which has been utilized as a hallmark of sperm capacitation over decades, showed different patterns in boar sperm capacitated *in vitro* from *ex vivo* and *in vivo* (Luno et al., 2013). In mice, pY is not required for sperm hyperactivation or fertility (Alvau et al., 2016; Tateno et al., 2013). Previous *in vitro* studies that represent the population average at a given time may or may not have observed molecular details of a small number of the most fertilizing sperm cells.

Capacitation involves extensive sperm remodeling that triggers cellular signaling cascades. Cholesterol shedding and protein modifications occur within the plasma membrane (Visconti et al., 1999; Vyklicka and Lishko, 2020). Cleavage and/or degradation of intracellular proteins by individual proteases and ubiquitin-proteasome system (UPS) also participate in the capacitation process (Honda et al., 2002; Kerns et al., 2016). Various capacitation-associated cellular signaling pathways that include cAMP/PKA activation followed by pY increase and rise in intracellular pH and calcium result in physiological outcomes such as acrosome reaction and motility changes (Balbach et al., 2018; Puga Molina et al., 2018). The sperm-specific CatSper Ca^{2+} channel forms multi-linear nanodomains on the flagellar membrane, functioning as a signaling hub that links these events and motility regulation during capacitation (Chung et al., 2014). Sperm from mice lacking CatSper genes are unable to control pY development and fail to migrate past the UTJ (Chung et al., 2014; Ho et al., 2009). The presence and integrity of CatSper nanodomains, probed by CatSper1, correlate with sperm ability to develop hyperactivated motility (Chung et al., 2017; Chung et al., 2014; Hwang et al., 2019). It is not known how these molecular and functional events are coordinated in the individual sperm cells within the physiological context.

Here, we reveal that most fertilizing mouse spermatozoa *in situ* are molecularly and functionally characterized by an intact CatSper channel, lack of pY, and reacted acrosomes. Using

70　biochemical and pharmacological analyses, we show that CatSper1 undergoes O-linked
71　glycosylation during sperm differentiation and maturation. Capacitation induces CatSper1
72　cleavage and degradation dependent on Ca^{2+} influx and protein phosphorylation cascades. We
73　find that CatSper1 processing correlates with pY development in the flagella among heterogenous
74　sperm cells capacitated *in vitro* and *in vivo*. We use *ex vivo* imaging and microdissection to show
75　that intact CatSper channel is indispensable for sperm to successfully reach the ampulla and for
76　the acrosome to react. Finally, we use newly developed 3D *in situ* molecular imaging strategies
77　and ANN approach to determine and quantify the molecular characteristics of sperm distributed
78　along the female reproductive tract. We demonstrate that all spermatozoa past the UTJ are
79　recognized by intact CatSper1 signals which are graded along the oviduct. These findings provide
80　molecular insight into dynamic regulation of Ca^{2+} signaling in selection, maintenance of the
81　fertilizing capacity, and elimination of sperm in the female reproductive tract.
82
83　**Results**
84
85　**CatSper1 undergoes post-translational modifications during sperm development and**
86　**maturation**
87　We previously found that the CatSper channel complex is compartmentalized within flagellar
88　membrane, creating linear Ca^{2+} signaling nanodomains along the sperm tail (Chung et al., 2017;
89　Chung et al., 2014; Hwang et al., 2019). Caveolin-1, a scaffolding protein in cholesterol-rich
90　microdomains, colocalizes with the CatSper channel complex but does not scaffold the
91　nanodomain (Chung et al., 2014). The molecular weight and amount of CatSper1, but not the
92　other CatSper subunits, declines during sperm capacitation (Chung et al., 2014; Figure 1B, D).
93　To better understand the processing of CatSper1, we first examined CatSper1 protein expression
94　in the testis and epididymis. Interestingly, the molecular weight of CatSper1 increases gradually
95　during sperm development and epidydimal maturation (Figure 1A; *upper*), indicating that
96　CatSper1 undergoes post-translational modifications. We next examined the nature of the
97　modifications. Block of tyrosine phosphatases by sodium orthovanadate or addition of specific
98　protein phosphatases, PP1 or PTP, does not change the molecular weight of CatSper1 (Figure1-
99　figure supplement 1A). In contrast, when sperm membrane was subjected to enzymatic
100　deglycosylation, O-glycosidase, but not PNGase F, shifts apparent molecular weight of CatSper1
101　to close to the CatSper1 band with the smallest molecular weight observed in testis (Figure 1A,
102　B, Figure1-figure supplement 1B). These data suggest that CatSper1 in sperm is not a
103　phosphoprotein but an O-linked glycosylated protein.
104
105　**CatSper1 resides in the subdomains of lipid rafts in mature sperm and processed during**
106　**capacitation**
107　Sucrose density gradient centrifugation identifies CatSper1 in lipid raft subdomains in mature
108　sperm (Figure 1C). Because cholesterol depletion destabilizes the plasma membrane during
109　sperm capacitation, one simple hypothesis is that the capacitation-associated changes in raft
110　stability and distribution (Nixon et al., 2007) render CatSper1 accessible to a protease activity.
111　Before inducing capacitation, CatSper1 is not processed in sperm cells, probably because the
112　CatSper1-targeting protease activity is normally not in the immediate vicinity to the CatSper
113　nanodomains in the flagellar membrane (Figure 1-figure supplement 1C, E). Supporting this

114 notion, the protease activity readily cleaves CatSper1 by solubilizing the sperm membrane
115 fraction with Triton X-100 (Figure 1-figure supplement 1C).

116

117 **The CatSper1 N-terminus undergoes capacitation-associated degradation *in vitro***
118 We next investigated the location of CatSper1 cleavage and degradation using recombinant
119 CatSper1 proteins and sperm lysates. The CatSper1 antibody used in this study is raised against
120 the first N-terminal 150 amino acids of recombinant CatSper1 (Ren et al., 2001). C-terminal HA-
121 tagged full-length (FL) or N-terminal deleted (ND) recombinant CatSper1 are expressed in HEK
122 293T cells for pull-down and detection by western blot (Figure 1E, F). Solubilized sperm lysates
123 degrade FL-CatSper1 and result in increased detection of cleaved CatSper1 by HA antibody
124 (Figure 1G; *upper*). In contrast, protein levels of recombinant ND-CatSper1 are not affected by
125 incubation with sperm lysate (Figure 1G; *lower*). These results demonstrate that the cytoplasmic
126 N-terminal domain of CatSper1 is the target region for proteolytic activity in sperm cells. How is
127 the CatSper proteolytic activity regulated?

128

129 **CatSper1 degradation involves Ca^{2+} and phosphorylation-dependent protease activity**
130 At the molecular level, capacitation is initiated by HCO_3^- uptake, which activates soluble adenylyl
131 cyclase (sAC), resulting in increased cAMP levels. HCO_3^- also stimulates CatSper-mediated Ca^{2+}
132 entry into sperm cells by raising intracellular pH (Figure 1-figure supplement 1E). We thus
133 examined whether the proteolytic activity requires cAMP/PKA and/or Ca^{2+} signaling pathways.
134 Interestingly, adding a PKA inhibitor H89 or the St-Ht31 peptide, which abolishes PKA anchoring
135 to AKAP during sperm capacitation, accelerated CatSper1 degradation during sperm capacitation
136 (Figure 1H, Figure 1-figure supplement 1D). Consistently, calyculin A, a serine/threonine protein
137 phosphatase inhibitor, suppresses the capacitation-associated CatSper1 degradation. These
138 data suggest that regulation of the proteolytic activity targeting CatSper1 involves protein
139 phosphorylation cascades (Figure 1-figure supplement 1E). Interestingly, adding Ca^{2+} ionophore
140 A23178 to the sperm suspension was sufficient to induce CatSper1 processing even under non-
141 capacitating conditions that do not support changes in PKA activity (Figure 1I, J). Thus, a Ca^{2+}
142 dependent protease that is indirectly regulated by protein phosphorylation such as calpain (Ono
143 et al., 2016) may process CatSper1. We observed that calpain inhibitors prevent CatSper1 from
144 capacitation-associated degradation (Figure 1K).

145

146 **CatSper1 degradation correlates with pY development in sperm cells capacitated *in vitro***
147 The presence and integrity of the CatSper nanodomains, probed by CatSper1 antibody, is an
148 indicator of sperm capability to hyperactivate (Chung et al., 2017; Chung et al., 2014). Inducing
149 sperm capacitation *in vitro* results in a functionally heterogeneous sperm population in which no
150 more than ~15% of cells are hyperactivated (Neill and Olds-Clarke, 1987). This is because
151 individual sperm cells undergo time-dependent changes. The extent to which protein tyrosine
152 phosphorylation (pY) develops and CatSper1 degrades varies with individual sperm cells
153 capacitated *in vitro* (Figure 1J, Figure 2A-C). Notably, we find that sperm cells that maintain intact
154 CatSper1 develop capacitation-associated pY to a lesser degree *in vitro* (Figure 2B, C). This
155 finding is consistent with the reported phenotype of *CatSper1* knockout sperm that exhibit
156 potentiated pY during capacitation (Chung et al., 2014). Thus far, our results suggest that *in vitro*
157 capacitation generates a heterogeneous sperm population in which intact CatSper1 and pY

158 development are inversely correlated in sperm cells at the single cell level. These heterogeneous
159 sperm cells *in vitro* may reflect a collection of the time- and space-dependent changes that sperm
160 undergo in the oviduct (Chang and Suarez, 2012; Demott and Suarez, 1992).
161
162 **Sperm cells capacitated *in vivo* become heterogeneous along the female tract with distinct**
163 **molecular characteristics**
164 To assess molecular changes of CatSper1 and pY in the spatially distributed sperm populations
165 along the female reproductive tract, we performed microdissection of the female reproductive tract
166 mated with *Acr-EGFP/Su9-DsRed2* male mice (Hasuwa et al., 2010) 8 hr post coitus and flushed
167 out sperm cells from different regions. By subsequent immunostaining, we found that CatSper1
168 in the spermatozoa that passed the utero-tubal junction (UTJ) are arranged normally along the
169 tail, mostly protected from degradation, but in decreasing intensity and continuity more towards
170 UTJ (Figure 2D, Figure 1-figure supplement 1E). In striking contrast, pY is not detected in the
171 spermatozoa from the ampulla but appears in the oviductal sperm increasingly towards UTJ
172 (Figure 2E). Absence of EGFP reveals that spermatozoa from the ampulla are fully capacitated
173 and acrosome reacted (AR) but the those in the isthmus are undergoing AR (Figure 2D, F). *Ex*
174 *vivo* imaging of *Acr-EGFP/Su9-DsRed* sperm in the reproductive tract removed from mated
175 female mice reveals segment-specific patterns of the acrosome status (Figure 2F), consistent
176 with the previous observations that AR initiates in the mid-isthmus (Hino et al., 2016; Muro et al.,
177 2016) and reacted spermatozoa are able to penetrate the zona *in vivo* (Jin et al., 2011).
178 Interestingly, we found that a few *CatSper1^{-/-}* sperm cells that managed to arrive at the ampulla
179 are all not acrosome reacted (Figure 2G), supporting the notion that CatSper-mediated Ca^{2+}
180 signaling is required for sperm acrosome reaction (Stival et al., 2018). These results suggest that
181 escape of CatSper1 from the cleavage and subsequent degradation suppresses pY development,
182 enabling sperm to maintain hyperactivation capability, prime AR, and achieve the fertilization *in*
183 *vivo*.
184
185 **3D *in situ* molecular imaging of gametes in the female reproductive tract**
186 The physiological importance of tracing a small number of spermatozoa progressing to the
187 fertilization site prompted us to seek a method that enables direct molecular assessment of single
188 cells inside the intact female tract. We have adapted tissue clearing technologies to establish
189 three-dimensional (3D) *in situ* molecular imaging systems for fertilization studies (Figure 3, Figure
190 3 – figure supplement 1, Videos 1-6). We found that various tissue clearing methods (Chung et
191 al., 2013; Murray et al., 2015; Yang et al., 2014) are applicable to the reproductive organs from
192 both male and female mice to preserve gross morphology, and fine cellular and subcellular
193 structures. The cleared tissues preserved protein-based fluorescence and were compatible with
194 labeling with dye and antibodies; growing follicles inside the ovary, oviductal folds and multi-
195 ciliated epithelium, different stages of male germs cells in the seminiferous tubules of the testis
196 and the epididymis are readily detected after clearing and labeling (Figure 3A-C, Figure 3 – figure
197 supplement 1, Videos 1-6). 3D volume imaging of the whole cleared female tract well illustrates
198 the uterine and isthmic mucus and the labyrinths of passages sperm must navigate (Figure 3A,
199 B, Figure 3 – figure supplement 1B, C, Videos 3, 5, 6). Moreover, 3D rendering of the images and
200 digital reconstruction of oviductal surface and central lumen depicts continuous and non-disrupted
201 morphology (Figure 3D, E) consistent with reported dimensions and parameters (Stewart and

202   Behringer, 2012), validating the integrity of the processed oviduct.

203

204   We next combined tissue clearing with an *in vivo* sperm migration assay (Chung et al., 2014;
205   Yamaguchi et al., 2009) to molecularly analyze different sperm populations during the fertilization
206   process. Among tested clearing methods, we found that passive clearing of CLARITY-processed
207   reproductive tract from time-mated females retains the location and stability of gametes within the
208   track past UTJ (Figure 3F-I, Videos 4, 7, 8); whole-animal fixation by trans-cardiac perfusion
209   perturbs minimally and rapidly arrests all cellular function while tissue-hydrogel matrix fills the
210   lumen and provides supportive meshwork to prevent gamete loss during subsequent labeling
211   steps (Figure 3 – figure supplement 2). This new *in situ* imaging platform enables capturing a
212   moment of sperm-egg interaction; a spermatozoon that approaches a fertilized egg protruding the
213   2nd polar body in the ampulla is detected in a cleared female tract 8 h post coitus immunostained
214   by acetylated tubulin antibody (Figure 3F, G, Video 7). CatSper1 antibody specifically recognizes
215   sperm cells transfixed in cleared female tract (Figure 3H). Tissue clearing allows 3D volume
216   imaging of the female tract but does not compromise the resolution. Two linear CatSper1 domains
217   typically observed by confocal imaging are easily observed in the sperm cells inside an ampullar
218   region of the whole cleared female tract (Figure 3I). Thus, the integrity of CatSper1 in sperm cells
219   at different locations along the female tract can be subjected to quantitative analysis.

220

221   **Sperm cell that successfully reach the ampulla are CatSper1-intact and acrosome reacted**
222   With this new imaging strategy to detect sperm cells that remain transfixed in the female tract
223   (Figure 3), we investigated acrosome state and CatSper1 integrity in sperm populations directly
224   from the cleared tract of females 8h after mating, focusing on a few anatomically defined regions
225   (Figure 4). Based on the earlier results from micro-dissection or *ex vivo* imaging (Figure 2D-G),
226   we anticipated that sperm cells that successfully reach the ampulla would be CatSper1-intact and
227   acrosome reacted. As expected, most sperm cells located in the ampulla exhibit linearly arranged
228   intact CatSper1 and reacted acrosomes (Figure 4A, *upper*, Video 8). In the middle isthmus, both
229   CatSper1 and acrosome remain intact in most sperm cells, but mixed patterns are observed in
230   some cells (Figure 4A, *middle*, Video 8). Interestingly, acrosome is largely intact in the sperm
231   clusters in the proximal isthmus close to UTJ whereas CatSper1 is barely detected (Figure 4A,
232   *lower*, Video 8). This contrasts with the reduced but readily visible CatSper1 in the sperm from
233   the same region by microdissection (Figure 2D). It is possible that the relatively longer tissue
234   processing time and subsequent labeling could have contributed to lower the signal to noise ratio
235   to a certain degree. Notably, 3D volume imaging of this mid isthmus regions reveals sperm cells
236   aligned in one direction towards the ampulla, providing unprecedented insight into sperm taxis in
237   the fertilization process (Video 8). Our qualitative but semi-quantitative analyses suggest that
238   CatSper1 is largely protected from degradation once in the oviduct; acrosome reaction initiates in
239   the mid-isthmus and is completed in the ampulla before interacting with the oocytes (Figure 4B).
240   These results are consistent with our initial observations from microdissection and *ex vivo* imaging
241   studies (Figure 2D, F), validating the information obtained by our *in situ* molecular imaging
242   platform. Taken together, we conclude that intact CatSper1, lack of pY, and reacted acrosome
243   are molecular and functional signatures of most fertilizing spermatozoa in the physiological
244   context.

245

Automatic detection of sperm in the voluminous female tract using artificial neural network

Processing 3D volumetric fluorescent data presents a significant challenge; analyses of sperm in the female tract includes object identification in the voluminous specimen, object separation from background noise, and object alignment in three dimensions. To address these logistics problems, we took an advantage of the artificial neural network (ANN) approach for automatic localization and signal isolation. We performed a proof-of-principle investigation utilizing CatSper1 distributions in sperm cells from our 3D *in situ* molecular imaging (Figure 5). First, we manually annotated 3D fluorescent signatures of sperm, somatic nuclei and background noise from the original images. These signatures were placed in different abundance models in the ANN 3D training environments (Figure 5A, Figure 5 - figure supplement 1, Video 9) for subsequent ANN training using MatLab ANN module. We performed a supervised iteration process where the sperm locations were predefined in the training environments (Figure 5 - figure supplement 2A). We evaluated the performance of individual ANN according to their sensitivity and specificity in detecting sperm cells and somatic nuclei, and the abundance (voxel occupancy) of noise (Figure 5B, Figure 5 - figure supplement 2B, C). Detection sensitivity is chosen as a major parameter used to evaluate the ANN performance in the training environment simulated with the values similar to those in real samples. The specificity required for sperm detection is lower than the sensitivity, thus provides mainly empty analytical frames that are easily removed manually. After iteration and performance evaluation, we selected the best performing ANN and analyzed images from our experimental samples for which we manually counted sperm number (Figure 5C). The selected ANN is able to recognize all the sperm detected manually and the ANN sensitivity varies around 90% in individual samples (Figure 5-figure supplement 2C), validating the ANN performance. Furthermore, the false-negative detection of sperm all comes from the sperm with dubious signals in the antecedent human eye evaluation; the 90% of the ANN detected sperm expresses well recognizable CatSper1 fluorescent staining patterns (Figure 5C, Figure 5-figure supplement 3A).

In order to pair each CatSper1 signal containing tail with the head from the same cell in the subsequent analysis, we took the reverse approach to the environment production by removing the detected noise and somatic cell nuclei from the analytical frames (Figure 5-figure supplement 3B). The pre-processed CatSper1 fluorescent signal were then subjected to subsequent alignment, pattern linearization, and intensity detection (Figure 5D, Figure 5-figure supplement 3C). These steps make possible calculation and visual representation of the fluorescent intensity parameters along the sperm tail related to their CatSper1 integrity status (Figure 5E-G).

ANN-quantified CatSper1 signal reveals a molecular signature of successful sperm *in situ*

The quadrilateral and linear organization of the Ca^{2+} signaling nanodomains discovered by super-resolution imaging of CatSper1 (Figure 6A) is an indicator of a sperm cell's ability to hyperactivate and fertilize the egg *in vitro* (Chung et al., 2017; Chung et al., 2014). The present study demonstrates that incubating sperm cell under capacitating conditions *in vitro* induces CatSper1 cleavage and degradation, leading to a heterogeneous sperm population (Figures 1, 2). Building on our observations of sperm cells from microdissection, *ex vivo* imaging, and CLARITY-based *in situ* molecular imaging (Figures 2, 3, 4), we hypothesize that CatSper1 is a built-in countdown timer for sperm death and elimination in the female tract; CatSper1 cleavage and degradation,

290 triggered in a time- and space-dependent manner along the female tract, signals to end sperm
291 motility, and ultimately sets sperm lifetime *in vivo*. With our newly developed automated ANN
292 method to obtain high-quality 3D fluorescent images of CatSper1 in the sperm cells from cleared
293 female tract samples, we further tested this idea by quantitatively analyzing the CatSper1 signals
294 *in situ*.
295
296 Our *in situ* imaging platform offers the typical resolution that a confocal microscopy can provide;
297 two separated CatSper1 arrangement along the sperm tail (Chung et al., 2017) are detected
298 without any computational processing (Figure 3I, 4A). This encouraged us to develop an analytical
299 procedure to assess the status of CatSper1 quadrilateral and linear distributions. We isolated the
300 fluorescent signal from a proximal region of the principal piece close to the annulus where
301 CatSper1 signal is the most intense (Figure 6B). To superpose the individual cross-sectional
302 images according to the expected 4 intensity peaks, we aligned randomly oriented transversal-
303 projection images by placing the quadrant with the highest fluorescent intensity to upper right
304 corner (Figure 6B, *inset*). The aligned images were then superposed (Figure 6C) and used for
305 statistical purposes to represent quadrilateral arrangement of CatSper1 in individual sperm cells
306 (Figure 6D). The individually processed images of sperm cells from the oviductal regions close to
307 UTJ, middle isthmus, and ampulla, regions were again superposed to create cumulative diagrams
308 and heat maps corresponding to these regions (Figure 6E). They show quadrilateral distribution
309 of enriched CatSper1 signal more clearly from the sperm population in the ampulla compared to
310 the population in the oviduct close to UTJ (Figure 6E, G, H).
311
312 To further quantify and statistically analyze our outputs, we divided the pre-processed images of
313 individual sperm cells on 80 round areas (Figure 6 – figure supplement 1A) and calculated
314 fluorescent intensities among them. The quantified intensity from the 80 areas were plotted; the
315 observed 4 peaks (highest intensity) and valleys (lowest intensity) were used to calculate the delta
316 value among them to represent the quality of CatSper1 quadrilateral structure (Figure 6F). Our
317 quantitative analysis (Figure 6G, Figure 6 – figure supplement 1B) shows consistent results with
318 our previous semi-quantitative analysis by manual assignment of the CatSper1 patterns (Figure
319 4). Together with the whole tissue image processing (Figure 3E), the quantitative analysis clearly
320 visualizes that sperm populations located along the cleared oviduct have statistically different
321 CatSper1 quadrilateral intensity delta values (Figure 6H).
322

Discussion

324
CatSper1 as a molecular barcode for sperm maturation and transition in the female tract
326 Testicular spermatozoa undergo maturation and biochemical alterations in the intraluminal
327 environment of the epididymis (Cornwall, 2009). Glycan-modifying enzymes such as glycosidases
328 and glycosyltransferases are present in the epididymal luminal fluid (Tulsiani, 2003). Here we
329 have shown that CatSper1 in mouse sperm is an O-linked glycosylated protein with gradually
330 increasing molecular weight from the testis to the epididymis during male germ-cell development.
331 The different forms of native CatSper1 may represent different degrees of glycosylation.
332 Heterologously expressed CatSper1 cannot reach the plasma membrane, remaining instead at
333 the ER/Golgi (Chung et al., 2017; Chung et al., 2011; Ren et al., 2001). It is intriguing that the

334 molecular weight of recombinant CatSper1 is similar to one of the testicular forms of CatSper1
335 but bigger than that of the enzymatically deglycosylated and naked polypeptide. O-linked
336 glycosylation takes place in the cis-Golgi for secreted and transmembrane proteins after the
337 protein is folded (Rottger et al., 1998), suggesting that additional modification is required for native
338 CatSper1 to exit the Golgi. Determining the precise identity and modification site may help to
339 clarify the long-sought functional expression of the CatSper channel in heterologous systems. In
340 rodents, sialyltransferase displays maturation-associated quantitative changes (Ram et al., 1989;
341 Scully and Shur, 1988) and sperm lose sialic acid from the surface during capacitation (Ma et al.,
342 2012). Sperm glycoproteins promote sperm migration and survival in the female reproductive tract
343 (Ma et al., 2016). We speculate that mature CatSper1 in sperm contains terminal sialic acid
344 residues, consistent with the small drop in Catsper1 molecular weight during capacitation. The
345 dynamic sugar modifications on CatSper1 may serve as a binding site for decapacitation factors
346 and/or a recognition site during capacitation. Supporting this idea, it was previously shown that
347 mouse sperm lacking CatSper channel cannot pass through the UTJ (Chung et al., 2014; Ho et
348 al., 2009).

350 Capacitation-associated CatSper1 degradation is blocked by incubation with a 26S proteasome
351 inhibitor, MG-132 (Chung et al., 2014). Now we show that solubilized sperm membrane fraction
352 contains additional proteolytic activities that cleave within CatSper1 NTD. The proteolysis is
353 dependent on Ca^{2+} entry and PKA phosphorylation cascade. A member of calpains, the Ca^{2+}
354 dependent modulatory protease family, may cleave CatSper1, as their proteolytic activity can be
355 positively regulated by PKA (Goll et al., 2003). Among 15 calpain proteins identified in mammals
356 (Ono et al., 2016), calpain1 and calpain11 were previously detected in our sperm proteome
357 (Hwang et al., 2019). Intriguingly, we observed that Ca^{2+} influx by A23187 is sufficient to induce
358 CatSper1 processing under non-capacitating conditions that do not support PKA activation.
359 Increased Ca^{2+} level overrides the phosphorylation effect on calpain1 activity (Du et al., 2018).
360 Calpain11 might be similarly regulated to calpain1, as their domain structures and catalytic
361 residues are conserved (Ono et al., 2016). Since recombinant CatSper1 is cleaved more
362 specifically by sperm lysates, we propose that the testis-specific calpain11 (Ben-Aharon et al.,
363 2006) may target CatSper1.

365 The effect of CatSper1 truncation on channel activity and sperm motility remains to be determined
366 in future studies. CatSper1 truncation may be coordinated with molecular changes of other
367 CatSper subunits. For example, the protein level of CatSper2, but not CatSper3 or 4, also
368 decreases after capacitation when probed with the antibody recognizing its C-terminal domain
369 (CTD) (Figure 1; Chung et al., 2014). Since the cytoplasmic modulatory subunits, CatSperζ and
370 Efcab9, mainly interact with the channel pore (Hwang et al., 2019), specific processing of the
371 intracellular domains of pore subunits could alter the interactions and subsequent channel activity.
372 Sperm that successfully navigate to the fertilization site in the female reproductive tract and
373 interact with the egg are recognized by intact CatSper1. CatSper1 processing may lead to a loss
374 of control in hyperactivation and eventually end sperm life.

376 **Physiological function of capacitation-associated tyrosine phosphorylation and acrosome**
377 **reaction**

378 An increase in pY is one of the various capacitation-associated parameters observed from *in vitro*
379 capacitated sperm cells (Visconti et al., 1995). Subsequently, pY was observed in the flagellum
380 of mouse and human sperm interacting with the oocyte in the medium that supports sperm
381 capacitation and fertilization *in vitro* (Sakkas et al., 2003; Urner et al., 2001). This correlation of
382 pY and the zona binding previously established pY as an indicator of successful sperm
383 capacitation. More recently, however, different observations have been made with *in vivo*
384 approaches. In sows inseminated close to ovulation, spermatozoa found in the UTJ exhibited
385 more phosphorylation in the flagella than those bound to oviductal epithelial cells (OEC), where
386 pY was limited to the equatorial region in the sperm head or no pY was observed (Luno et al.,
387 2013). In mice, the testis-specific tyrosine kinase, Fer, is demonstrated as a master kinase for
388 capacitation-associated pY (Alvau et al., 2016). Surprisingly, homozygous *Fer*-mutant male mice
389 are fertile even though their sperm do not develop pY. All together, these results lead to a new
390 interpretation of the physiological significance of pY: successful sperm capacitation does not
391 require pY development. Determining the precise time and place of pY development in sperm *in*
392 *situ* would help to elucidate its function in sperm capacitation and fertilization. Here we have
393 shown that sperm, which have capacitated *in vivo* and successfully migrated to the ampulla, are
394 characterized, not only by intact CatSper1, but also by lack of pY development and reacted
395 acrosome. These results coincide with our observations from *in vitro* capacitated sperm cells and
396 other previous studies; pY development inversely correlates with CatSper1 integrity at the single
397 cell level (Figure 2); genetic and pharmacological ablation of Ca^{2+} entry potentiates pY (Chung et
398 al., 2014; Navarrete et al., 2015); AR occurs in mid-isthmus before contacting an oocyte ZP (Hino
399 et al., 2016; Jin et al., 2011; Muro et al., 2016).
400
401 Sperm remaining in the female reproductive tract need to be eliminated after fertilization. They
402 may undergo apoptosis and phagocytosis in the female reproductive tract (Aitken and Baker,
403 2013; Chakraborty and Nelson, 1975) and/or become lost in the peritoneal cavity (Mortimer and
404 Templeton, 1982). pY is reported to mediate apoptosis in immune cells (Yousefi et al., 1994) and
405 cancer cells (Liu et al., 1994). We propose that capacitation-associated global pY development
406 represents degenerating sperm which might concomitantly lose motility. It is intriguing that
407 capacitation-associated reactive oxygen species (ROS) generation activates intrinsic apoptotic
408 cascade and compromises sperm motility (Koppers et al., 2011). Consistent with this idea, ROS
409 inactivates protein tyrosine phosphatase (Tonks, 2005) and enhances pY development in sperm
410 (Aitken et al., 1998). Inhibition of PKA anchoring to AKAPs, which induces CatSper1 truncation
411 and degradation, also suppresses acrosome reaction in capacitating sperm cells *in vitro* (Stival et
412 al., 2018). Thus, CatSper-mediated Ca^{2+} signaling directly or indirectly contributes to sperm
413 acrosome reaction in the female tract. Future work will determine molecular mechanisms by which
414 CatSper channel activity fine-tunes Ca^{2+} signaling to regulate hyperactivated motility, as well as
415 how the Ca^{2+} signaling is linked to coordinate acrosome reaction.
416
417 **New *in situ* molecular imaging platform for the study of fertilization and reproduction**
418 Successful development of *in vitro* capacitation and fertilization systems provided fundamental
419 insights into sperm capacitation, fertilization and early embryogenesis. On the other hand, it is
420 evident that the *in vitro* systems have limitations. Sperm numbers required for IVF are much higher
421 than those observed at the fertilization site *in vivo* (Suarez, 2006). Sperm capacitated *in vitro* do

422 not encounter the anatomically and spatially distinct environment of the female reproductive tract,
423 for example, missing their interaction with the oviductal epithelial cells. *In vitro* capacitation also
424 lacks secretory factors from the male and female reproductive tracts that can affect the surface
425 protein dynamics during the capacitation process (Flesch and Gadella, 2000). Mouse models that
426 typically use epidydimal sperm for *in vitro* studies do not contain secretions from male glands.
427 This is in contrast with ejaculated sperm from human and domestic animals. Recent studies have
428 observed sperm behavior in the physiological context through *ex vivo* imaging of sperm in the
429 mouse and bovine oviducts under transillumination (Hino and Yanagimachi, 2019; Ishikawa et al.,
430 2016; Kolle et al., 2009; Muro et al., 2016). Yet this technique is limited in providing molecular
431 information at a single cell level, as live imaging is not easily amenable to direct molecular labeling
432 and 3D volume imaging.

434 Here, we report new systems to molecularly examine individual sperm cells capacitated *in vivo*.
435 Polymerization of the hydrogel-embedded time-mated female reproductive tract followed by
436 passive clearing provides a stable meshwork to minimally disturb the original location of sperm
437 cells inside the female tract. This approach allowed us to assess the fine organization of CatSper
438 nanodomains in the sperm cells distributed along the female reproductive tract. We showed that
439 both the intensity and the quadrilateral detection of the domains probed by CatSper1 appear as
440 the common pattern of sperm reaching the ampulla and potentially fertilizing the oocyte. The
441 experimental outputs complement the molecular and functional information of sperm released
442 from micro-dissected female tracts and *ex vivo* imaging, identifying molecular and functional
443 signatures of fertilizing sperm in the physiological context. Furthermore, we demonstrate the
444 efficacy of topological heat-map representations of cumulative results by automatic sperm
445 detection and image post-processing and averaging; this method provides statistically robust
446 presentation and interpretation of the volumetric image data.

448 The present study opens up new horizons to microscopically visualize and analyze molecular
449 events in single sperm cells that achieve fertilization. This will allow us to better understand
450 physiologically relevant cellular signaling pathways directly involved in fertilization. We also have
451 illustrated that the same approach of tissue-clearing based 3D *in situ* molecular imaging is
452 applicable to study gametogenesis *in situ*. Future areas for investigations as natural extensions
453 of the current study are gameto-maternal interaction, development, transport, and implantation of
454 early embryos and maternal-fetal communication. Developing gamete-specific antibodies and/or
455 knockout validated antibodies to probe molecular abundancy and dynamics *in situ* and post-
456 processing tools for various parameters will be critical to this end.

458 **Materials and Methods**

460 **Animals**
461 *CatSper1*-null (Ren et al., 2001) and *Su9-DsRed;Acr-EGFP* (Hasuwa et al., 2010) mice were
462 generated in the previous study and maintained on a C57BL/6 background. *Su9-DsRed;Acr-*
463 *EGFP* mice were crossbred with *CatSper1*-null mice to generate *Su9-DsRed;Acr-EGFP*
464 *CatSper1*-null mice. WT C57BL/6 and B6D2F1 male and CD1 female mice were purchased from
465 Charles River Laboratories (Wilmington, MA) and Jackson laboratory (Bar Harbor, ME). Mice

466 were cared in accordance with guidelines approved by the Yale Animal Care and Use
467 Committees.

468

Mammalian Cell Lines

470 HEK293T and COS-7 cells were purchased from ATCC. They were cultured in DMEM (GIBCO)
471 supplemented with 10% FBS (Thermofisher) and 1x Pen/Strep (GIBCO) at 37 °C, 5% CO_2
472 condition. Cultured cells were used to express recombinant proteins (HEK293T cells) or make
473 total cell lysates (COS-7 cells).

474

Antibodies and Reagents

476 In-house rabbit polyclonal CatSper1 (Ren et al., 2001), CatSper3 (Qi et al., 2007), CatSperε
477 (Chung et al., 2017) antibodies were described previously. Polyclonal CA-IV antibody (M-50) was
478 purchased from Santacruz. Monoclonal antibodies were purchased from BD Biosciences: anti-
479 caveolin1 (clone 2297); EMD Milipore: anti-phosphotyrosine (clon4G10,) anti- acetylated tubulin
480 (clone 6-11B-1), anti-HA agarose (clone HA-7), and Cell Signaling Technology: anti-ubiquitin
481 (clone P4D1), β-actin (clone 13E5), and HA (clone C29F4) . HRP-conjugated goat anti-rabbit IgG
482 and goat anti-mouse IgG were from Jackson Immunoresearch. PNA-Alexa 568, WGA-Alexa 555,
483 WGA-Alexa 647, goat anti-mouse IgG (Alexa 488 or 647), and goat anti-rabbit IgG (Alexa 568 or
484 Alexa 647) were from Invitrogen. H89, calyculin A, and Ca^{2+} ionophore A23178 were purchased
485 from Calbiochem. ST-Ht31 was from Promega. Calpain inhibitor II and III were from Enzo life
486 science. All other chemicals were from Sigma-Aldrich unless indicated.

487

Epididymal sperm collection and *in vitro* capacitation

489 Sperm cells were released from caput, corpus, or cauda regions of epididymis in M2 medium
490 (EMD Millipore). To induce capacitation, sperm from caudal epididymis were incubated in human
491 tubular fluid (HTF) medium or M16 (EMD Milipore) containing 25 mM sodium bicarbonate at 37
492 °C, 5% CO_2 condition at 2 x 10^6 cells/ml concentration for indicated time. Sperm cells were
493 incubated under capacitating conditions with or without the following chemicals: H89 (50 μM), ST-
494 Ht31 (10 μM), Calyculin A (100 nM), calpain inhibitor I (20 μM), calpain inhibitor II (20 μM), or
495 calpain inhibitor III (20 μM). Sperm cells suspended in M2 medium (2 x 10^6 cells/ml) were
496 incubated with A23187 (10 μM) to induce Ca^{2+} influx under non-capacitating conditions.

497

Molecular Cloning

499 NEB10β bacterial strain (NEB) was used for the molecular cloning. Genomic regions encoding
500 full-length (FL, 1-686 aa) and N-terminal domain deleted (ND, 345-686 aa) mouse CatSper1 were
501 amplified from mouse CatSper1 expression vector (Hwang et al., 2019). The PCR products were
502 subcloned into pcDNA3.1(-) vector using NEBuilder HiFi DNA Assembly (NEB) to express the
503 recombinant proteins tagged with HA at C-terminus (*pcDNA3.1(-)-FL-CatSper1-HA* and
504 *pcDNA3.1(-)-ND-CatSper1-HA*.

505

Recombinant protein expression

507 HEK293T cells were transfected with constructs encoding FL-CatSper1 or ND-CatSper1 to
508 express the recombinant proteins transiently. Polyethyleneimine was used for the transfection
509 following the manufacturer's instruction as previously.

510
511 **Protein Preparation and Western blot.**
512 *Total Protein Extraction*
513 Total proteins were extracted from sperm, testis, and cultured mammalian cells as previously
514 described (Hwang et al., 2019). In short, collected epididymal sperm cells were washed with PBS
515 and lysed in 2X LDS sampling buffer for 10 min at room temperature with agitation (RT). The
516 whole sperm lysates were centrifuged at 14,000 x g for 10 min at 4 °C. Testes were homogenized
517 in 0.32M sucrose and centrifuged at 1,000 x g for 10 min at 4 °C to remove cell debris and nuclei.
518 1% Triton X-100 in PBS containing protease inhibitor cocktail (cOmplete^{TM}, EDTA-free, Roche)
519 was added to the cleared homogenates to make total testis lysate. The lysates were centrifuged
520 at 4 °C, 14,000 x g for 30 min and the supernatant was used for the downstream experiments.
521 Transfected HEK29T cells and COS-7 cells were washed and lysed with 1% Triton X-100 in PBS
522 with protease inhibitor cocktail (Roche) at 4 °C for 1 hr. Cell lysates were centrifuged at 14,000 x
523 g for 30 min. All the solubilized protein lyates from the sources described above were reduced by
524 adding dithiothreitol (DTT) to 50 mM and denature by heating at 75 °C for 5 min (testis and
525 cultured cells) or 10 min (sperm).
526
527 *Discontinuous Sucrose Density Gradient Centrifugation*
528 Discontinuous sucrose density gradient centrifugation was performed as previously described
529 (Kaneto et al., 2008). To isolate and solubilize membrane fraction without using a detergent,
530 cauda epididymal sperm cells washed and suspended in PBS (1.0 x 10^8 cells/ml) were sonicated
531 3 times for 1 sec each. Sonicated sperm cells were then centrifuged at 5,000 x g for 10 min at 4
532 °C and the solubilized membrane fraction in supernatant was collected. The solubilized
533 membrane fraction was pelleted by ultracentrifugation at 100,000 x g for 1 hr at 4 °C and
534 resuspended with PBS. The membrane suspension was mixed with equal volume of 80 %
535 sucrose in PBS. A discontinuous sucrose gradient was layered with the 40%, 30 %, and 5 %
536 sucrose solution from bottom to top in a tube discontinuously. The gradient was ultracentrifuged
537 at 200,000 x g for 20 hr at 2 °C. Proteins collected from each fraction were precipitated with 5 %
538 of trichloroacetic acid, ethanol washed, and dissolved in SDS sampling buffer.
539
540 *Dephosphorylation of Sperm Membrane Proteins*
541 Sperm membrane fractions from 1 x 10^6 sperm cells prepared as above were treated with protein
542 phosphatase 1, (PP1, 0.1 unit; NEB), protein tyrosine phosphatase (PTP, 5 unit; NEB), or sodium
543 orthovanadate (Na$_3$VO$_4$, 1 mM; NEB) to test dephosphorylation of CatSper1. The membrane
544 fractions were incubated with the phosphatases or Na$_3$VO$_4$ in a reaction buffer containing 20mM
545 HEPES, 0.1 mM EDTA and 0.1mM DTT at 30 °C for the indicated times. The isolated sperm
546 membrane was solubilized by adding Triton X-100 to final 0.1% in PBS (PBS-T) for the indicated
547 times at RT.
548
549 *Enzymatic Deglycosylation*
550 Glycosylation of CatSper1 from cauda sperm was tested using PNGase F (Sigma-Aldrich) and
551 O-glycosidase (NEB). Sperm cells were washed with 1x reaction buffer for each enzyme by
552 centrifugation at 800 x g for 3 min. Sperm pellets were re-suspended with each 1x reaction buffer
553 (20 mM or 50 mM sodium phosphate, pH7.5 for PNGase F and O-glycosidase, respectively) and

554   followed by sonication and centrifugation to collect sperm membrane fraction as described above.
555   Collected supernatants were incubated with denaturation buffer at 100 °C for 5 min to denature
556   glycoproteins before subject to enzymatic deglycosylation. The denatured sperm membrane
557   fractions were incubated with detergent buffer (0.75% IGEPAL CA for PNGase F; 1% NP-40 for
558   O-glycosidase) and each glycosidase at 37 °C for 1 hr. All the enzyme-treated samples were
559   mixed with LDS sampling buffer and denatured after adding DTT to 50 mM at 75 °C for 2 min.
560
561   *In Vitro Proteolysis with Sperm Lysate*
562   Proteolysis of the recombinant CatSper1 protein by sperm lysate were performed as previously
563   described (Chung et al., 2014). Solubilized recombinant FL-CatSper1 and ND-CatSper1 were
564   pulled-down with anti-HA agarose (EMD Millipore) for 1 hr at RT. The enriched recombinant
565   proteins were incubated with 30 μl of sperm lysates solubilized from 3.0 x 10^5 sperm cells at 37
566   °C for the indicated times. Sperm lysates were prepared by sonication and incubation in PBS-T
567   without protease inhibitor at 4 °C for 1 hr. After the incubation, mixture of recombinant protein and
568   sperm lysates were mixed to 2X LDS sampling buffer and denatured by adding DTT to 50 mM at
569   75 °C for 10 min.
570
571   **Western Blot**
572   Denatured protein samples were subjected to SDS-PAGE. Rabbit polyclonal CatSper1 (2 μg/ml),
573   CatSper3 (2 μg/ml), CatSperϵ (1.6 μg/ml), and CAIV (1:500) antibodies and monoclonal HA (clone
574   C29F4; 1:2,000), caveolin1 (clone 2297, 1:500), acetylated tubulin (clone 6-11B-1; 1:20,000),
575   phosphotyrosine (clone 4G10; 1:1,000), and ubiquitin (clone P4D1; 1:1,000) antibodies were used
576   for western blot. Anti-mouse IgG-HRP (1:10,000) and anti-rabbit IgG-HRP (1:10,000) were used
577   for secondary antibodies.
578
579   **Sperm Migration assay**
580   Sperm migration assay was performed as previously described (Chung et al., 2014). Briefly,
581   female mice were introduced to single-caged *Su9-DsRed;Acr-EGFP* males for 30 min and
582   checked for vaginal plug. Whole female reproductive tracts were collected 8 h post-coitus and
583   subjected to *ex vivo* imaging to examine spermatozoa expressing reporter genes in the tract
584   (Eclipse TE2000-U, Nikon).
585
586   **Collection of *in vivo* Capacitated Sperm**
587   Female reproductive tracts from timed-mated females to *Su9-DsRed;Acr-EGFP* or *Su9-*
588   *DsRed;Acr-EGFP CatSper1*-null males were collected 8 h post coitus. Sperm cells were released
589   by micro-dissection of female reproductive tract followed by lumen flushing of each tubal segment
590   (cut into ~ 1-2 mm pieces). Each piece was placed in 50 μl of PBS on glass coverslips and the
591   intraluminal materials were fixed immediately by air-dry followed by 4% PFA in PBS. Ampulla and
592   uterine tissue close to UTJ were placed in 100 μl of PBS and vortexed briefly to release the sperm
593   within the tissues. Fixed sperm cells were subjected to immunostaining.
594
595   **Sperm immunocytochemistry**
596   Non-capacitated or *in vitro* capacitated sperm cells on glass coverslips were washed with PBS
597   and fixed with 4% paraformaldehyde (PFA) in PBS at RT for 10 minutes. Fixed samples were

598 permeabilization with PBS-T for 10 min and blocked with 10% normal goat serum in PBS for 1 hr
599 at RT. Blocked sperm cells were stained with primary antibodies, anti-CatSper1 (10 μg/ml) and
600 anti-phosphotyrosine (1:1,000), at 4 °C for overnight, followed by staining with secondary
601 antibodies for 1 hr at RT. Hoechst was used for counterstaining sperm head. Sperm cells were
602 mounted (Vectashield, Vector Laboratories) and imaged with confocal microscopes (Zeiss
603 LSM710 Elyra P1 and Olympus Fluoview 1000).
604
605 **Tissue clearing and molecular labeling of the cleared tissues**
606 *CLARITY*
607 All 3D volume images from the main figures (Figures 3 and 4) were taken from female tracts
608 subjected to CLARITY method (Chung et al., 2013) with slight modification by clearing tissue-
609 hydrogel passively without involving electrophoresis. Timed-mated females (8 h post coitus) and
610 males were subjected to transcardiac perfusion using peristaltic pump. The mice were perfused
611 with each 20 ml of ice-cold PBS followed by freshly prepared hydrogel monomer solution (4%
612 acrylamide, 2% Bis-acrylamide, 0.25% Azo-inhibitor (VA-044, Wako), 4% PFA in PBS). The whole
613 female tract or testis-hydrogel were dissected from animals after perfusion and placed in 10 ml of
614 fresh hydrogel monomer solution for post-fixation. The collected tissues in monomer solution were
615 heated at 37 °C with degassing for 15 min, followed by incubation at 37 °C for 2-3 h for tissue
616 gelation. The gelated tissues were washed with clearing solution containing 200 mM boric acid
617 and 4% sodium dodecyl sulfate (pH8.5) three times for 24 h each by gentle rocking at 55 °C.
618 Cleared tissues were further washed with PBS-T for 24 h. The cleared female tracts were
619 subjected to dye- and/or immunolabeling: the cleared tissues were incubated with CatSper1 (7
620 μg/ml) or AcTub (1:100) antibodies in PBS-T for overnight at RT, followed by washing with PBS-
621 T for 24 h. Washed samples were stained with the secondary antibodies (1:500) overnight.
622 Fluorescence dye conjugated PNA or WGA were used to detect sugar residues (1:1,000) and
623 DAPI were used for counter staining (1:1000) in PBS-T. Stained tissues were washed and
624 refractive index matched in RIMS solution (Chung et al., 2013) overnight. The index-matched
625 samples were put on imaging chamber filled with RIMS solution and imaged. All cleared tissues
626 were imaged with laser scanning microscope (Zeiss LSM710 Elyra P1). EC plan-Neofluar 10x/0.3,
627 LD LCI Plan-Apochromat 40x1.2, and Plan-Apochromat 63x/1.4 objectives were used for imaging.
628 Tile scanning and z-stacking for volume imaging were carried out with functions incorporated in
629 Zen black 2012 SP2 (Carl Zeiss) and Zen blue 2011 SP1 software (Carl Zeiss) was used for 3D
630 rendering.
631 *X-CLARITY*
632 Ovary, testis, and epididymis images (Figure 3 – figure supplement 1A, D-I) were taken from X-
633 CLARITY method, following manufacturer's instruction (Logos biosystems). Animals
634 transcardially fixed with 4% PFA were post fixed in the fresh fixative for 4-6 h. The post-fixed
635 tissues were then immersed in a modified hydrogel solution (4% acrylamide, 0.25% Azo-inhibitor
636 (VA-044, Wako), 4% PFA in PBS) for 4-6 h. The samples were degassed and polymerized as
637 described in CLARITY method. The gelated tissues were washed with PBS and placed in
638 electrophoretic tissue clearing (ETC) chamber. Tissues in the ETC chamber were cleared by
639 clearing solution described above with active electrophoretic forcing of tissue for 6-8 hr. Cleared
640 tissues were washed and stained with β-actin and WGA.
641 *PACT-PRESTO*

642   3D volume images of the oviduct and UTJ (Figure 3 – figure supplement 1B, C) were obtained
643   from the female tract cleared by modified passive ACT-PRESTO (Lee et al., 2016) without
644   involving electrophoretic clearing. In brief, female tracts were fixed in 4% PFA by transcardiac
645   perfusion, followed by post-fixation in fresh fixative solution for 4-6 hours at 4 °C. The post-fixed
646   samples were incubated in the modified hydrogel monomer solution without additional fixative
647   (4% acrylamide, 0.25% Azo-inhibitor in PBS) 4-6 hours at 4 °C. The samples were degassed and
648   polymerized at 37 °C as described in CLARITY method. Hydrogel-infused tissues were cleared
649   with the clearing solution. The cleared tissues were washed with PBS overnight at RT and
650   facilitated labeling is achieved by vacuum-applied negative pressure.
651   *SWITCH*
652   3D volume images of testis (Figure 3 – figure supplement 1F) were taken from male mice
653   transcardially perfused and cleared by SWITCH method (Murray et al., 2015). Fixed testes by
654   SWITCH fixative (4% PFA, 1% glutaraldehyde (GA) in PBS) were washed with PBS-T and
655   quenched by 4% glycine and 4% acetamide in PBS at 37 °C for overnight. The quenched samples
656   were passively cleared with SWITCH solution (200 mM SDS, 20 mM Na_2SO_3, 10 mM NaOH, pH
657   9.0) 2 times at 60 °C for 3 h each. The cleared tissues were washed with PBS-T for 12-24 h at 37
658   °C and incubated with refraction index-matching solution (RIMS: 29.4% diatrizoic acid, 23.5% n-
659   methyl-d-glucamine, 32.4% iodixanol). The index matched samples were mounted and imaged.
660
661   **Artificial neural network (ANN) image processing**
662   The overall strategy for the artificial neural network (ANN) image processing is described in Figure
663   4 – figure supplement 2A. The individual signal patterns (sperm, somatic cell nuclei, and noise)
664   were isolated from the original volume images using Zen Blue (Carl Zeiss) and IMARIS software
665   (Oxford instruments) and exported as .obj/.fbx files. The isolated signal patterns were used to
666   generate 3D training environments for ANN by importing different abundancies of the individual
667   components (Figure 4 – Supplementary figure 1) to the 3D environment operating system,
668   Blender 2.79 (https://www.blender.org/); the individual 3D training environment (~10^4) generated
669   together with the exactly defined coordinates of individual components were exported as
670   .obj/.fbx/Notepad++ files. The ANN training environments were used to develop the ANN
671   detecting the sperm *in situ*. The ANN training was carried out using MATLAB 9.3 (R2017b)
672   software ANN toolbox. The input to the ANN would be virtual *z*-stacks of the produced training
673   environments. The isolated sperm signal patterns were used as as target signature. The
674   supervised training process was performed by comparing the vector coordinates of the individual
675   sperm signatures in the output with the pre-defined vector coordinates of the signatures in the
676   input. This approach also enabled us to evaluate the ANN performance and to quantify signature
677   detection sensitivity and specificity. ANNs with the best performance in detecting the sperm
678   signature were subsequently applied to detect the sperm fluorescent signatures and their post-
679   processing in real volumetric data. In the real environments, selected ANNs showed both
680   sensitivity and specificity around 90%.
681
682   **Statistical analyses**
683   Statistical analyses were carried out with one-way analysis of variance (ANOVA) with Tukey post
684   hoc test. Differences were considered significant at $p < 0.05$. For ANN analysis, both parametric
685   (ANOVA; Tukey post hoc) and non-parametric (KW-ANOVA) tests were carried out to evaluate

686   the presented differences; both tests resulted in the same significance output with differences
687   considered significant at $p < 0.05$.
688

Acknowledgements

695

Competing interests

697   The authors declare that no competing interests exits.

References

Aitken, R., Harkiss, D., Knox, W., Paterson, M., and Irvine, D. (1998). A novel signal transduction cascade in capacitating human spermatozoa characterised by a redox-regulated, cAMP-mediated induction of tyrosine phosphorylation. Journal of Cell Science *111*, 645-656.

Aitken, R.J., and Baker, M.A. (2013). Oxidative stress, spermatozoa and leukocytic infiltration: relationships forged by the opposing forces of microbial invasion and the search for perfection. Journal of reproductive immunology *100*, 11-19.

Alvau, A., Battistone, M.A., Gervasi, M.G., Navarrete, F.A., Xu, X., Sanchez-Cardenas, C., De la Vega-Beltran, J.L., Da Ros, V.G., Greer, P.A., Darszon, A.*, et al.* (2016). The tyrosine kinase FER is responsible for the capacitation-associated increase in tyrosine phosphorylation in murine sperm. Development *143*, 2325-2333.

Austin, C.R. (1951). Observations on the penetration of the sperm in the mammalian egg. Aust J Sci Res B *4*, 581-596.

Balbach, M., Beckert, V., Hansen, J.N., and Wachten, D. (2018). Shedding light on the role of cAMP in mammalian sperm physiology. Mol Cell Endocrinol *468*, 111-120.

Ben-Aharon, I., Brown, P.R., Shalgi, R., and Eddy, E.M. (2006). Calpain 11 is unique to mouse spermatogenic cells. Molecular Reproduction and Development: Incorporating Gamete Research *73*, 767-773.

Chakraborty, J., and Nelson, L. (1975). Fate of surplus sperm in the fallopian tube of the white mouse. Biol Reprod *12*, 455-463.

Chang, H., and Suarez, S.S. (2012). Unexpected flagellar movement patterns and epithelial binding behavior of mouse sperm in the oviduct. Biology of reproduction *86*, 140, 141-148.

Chang, M.C. (1951). Fertilizing capacity of spermatozoa deposited into the fallopian tubes. Nature *168*, 697-698.

Chung, J.J., Miki, K., Kim, D., Shim, S.H., Shi, H.F., Hwang, J.Y., Cai, X., Iseri, Y., Zhuang, X., and Clapham, D.E. (2017). CatSperzeta regulates the structural continuity of sperm Ca(2+) signaling domains and is required for normal fertility. Elife *6*.

Chung, J.J., Navarro, B., Krapivinsky, G., Krapivinsky, L., and Clapham, D.E. (2011). A novel gene required for male fertility and functional CATSPER channel formation in spermatozoa. Nat Commun *2*, 153.

Chung, J.J., Shim, S.H., Everley, R.A., Gygi, S.P., Zhuang, X., and Clapham, D.E. (2014). Structurally distinct Ca(2+) signaling domains of sperm flagella orchestrate tyrosine phosphorylation and motility. Cell *157*, 808-822.

Chung, K., Wallace, J., Kim, S.-Y., Kalyanasundaram, S., Andalman, A.S., Davidson, T.J., Mirzabekov, J.J., Zalocusky, K.A., Mattis, J., and Denisin, A.K. (2013). Structural and molecular interrogation of intact biological systems. Nature *497*, 332-337.

Cornwall, G.A. (2009). New insights into epididymal biology and function. Human reproduction update *15*, 213-227.

Demott, R.P., and Suarez, S.S. (1992). Hyperactivated sperm progress in the mouse oviduct. Biology of reproduction *46*, 779-785.

Du, M., Li, X., Li, Z., Shen, Q., Wang, Y., Li, G., and Zhang, D. (2018). Phosphorylation regulated by protein kinase A and alkaline phosphatase play positive roles in μ-calpain activity. Food chemistry *252*, 33-39.

Flesch, F.M., and Gadella, B.M. (2000). Dynamics of the mammalian sperm plasma membrane in the process of fertilization. Biochimica et Biophysica Acta (BBA)-Reviews on Biomembranes *1469*, 197-235.

Fujihara, Y., Miyata, H., and Ikawa, M. (2018). Factors controlling sperm migration through the oviduct revealed by gene-modified mouse models. Exp Anim *67*, 91-104.

Goll, D.E., Thompson, V.F., Li, H., Wei, W., and Cong, J. (2003). The calpain system. Physiological reviews.

745   Hasuwa, H., Muro, Y., Ikawa, M., Kato, N., Tsujimoto, Y., and Okabe, M. (2010). Transgenic mouse sperm
746   that have green acrosome and red mitochondria allow visualization of sperm and their acrosome
747   reaction in vivo. Experimental animals *59*, 105-107.
748   Hino, T., Muro, Y., Tamura-Nakano, M., Okabe, M., Tateno, H., and Yanagimachi, R. (2016). The Behavior
749   and Acrosomal Status of Mouse Spermatozoa In Vitro, and Within the Oviduct During Fertilization after
750   Natural Mating. Biol Reprod *95*, 50.
751   Hino, T., and Yanagimachi, R. (2019). Active peristaltic movements and fluid production of the mouse
752   oviduct: their roles in fluid and sperm transport and fertilizationdagger. Biol Reprod *101*, 40-49.
753   Ho, K., Wolff, C.A., and Suarez, S.S. (2009). CatSper-null mutant spermatozoa are unable to ascend
754   beyond the oviductal reservoir. Reprod Fertil Dev *21*, 345-350.
755   Honda, A., Siruntawineti, J., and Baba, T. (2002). Role of acrosomal matrix proteases in sperm–zona
756   pellucida interactions. Human Reproduction Update *8*, 405-412.
757   Hwang, J.Y., Mannowetz, N., Zhang, Y., Everley, R.A., Gygi, S.P., Bewersdorf, J., Lishko, P.V., and Chung,
758   J.J. (2019). Dual Sensing of Physiologic pH and Calcium by EFCAB9 Regulates Sperm Motility. Cell *177*,
759   1480-1494 e1419.
760   Ishikawa, Y., Usui, T., Yamashita, M., Kanemori, Y., and Baba, T. (2016). Surfing and Swimming of
761   Ejaculated Sperm in the Mouse Oviduct. Biol Reprod *94*, 89.
762   Jin, M., Fujiwara, E., Kakiuchi, Y., Okabe, M., Satouh, Y., Baba, S.A., Chiba, K., and Hirohashi, N. (2011).
763   Most fertilizing mouse spermatozoa begin their acrosome reaction before contact with the zona
764   pellucida during in vitro fertilization. Proc Natl Acad Sci U S A *108*, 4892-4896.
765   Kaneto, M., Krisfalusi, M., Eddy, E.M., O'Brien, D.A., and Miki, K. (2008). Bicarbonate-induced
766   phosphorylation of p270 protein in mouse sperm by cAMP-dependent protein kinase. Mol Reprod Dev
767   *75*, 1045-1053.
768   Kerns, K., Morales, P., and Sutovsky, P. (2016). Regulation of Sperm Capacitation by the 26S Proteasome:
769   An Emerging New Paradigm in Spermatology. Biol Reprod *94*, 117.
770   Kolle, S. (2015). Transport, Distribution and Elimination of Mammalian Sperm Following Natural Mating
771   and Insemination. Reprod Domest Anim *50 Suppl 3*, 2-6.
772   Kolle, S., Dubielzig, S., Reese, S., Wehrend, A., Konig, P., and Kummer, W. (2009). Ciliary transport,
773   gamete interaction, and effects of the early embryo in the oviduct: ex vivo analyses using a new digital
774   videomicroscopic system in the cow. Biol Reprod *81*, 267-274.
775   Koppers, A.J., Mitchell, L.A., Wang, P., Lin, M., and Aitken, R.J. (2011). Phosphoinositide 3-kinase
776   signalling pathway involvement in a truncated apoptotic cascade associated with motility loss and
777   oxidative DNA damage in human spermatozoa. Biochemical Journal *436*, 687-698.
778   Lee, E., Choi, J., Jo, Y., Kim, J.Y., Jang, Y.J., Lee, H.M., Kim, S.Y., Lee, H.J., Cho, K., Jung, N.*, et al.* (2016).
779   ACT-PRESTO: Rapid and consistent tissue clearing and labeling method for 3-dimensional (3D) imaging.
780   Sci Rep *6*, 18631.
781   Liu, Y., Bhalla, K., Hill, C., and Prlest, D.G. (1994). Evidence for involvement of tyrosine phosphorylation
782   in taxol-induced apoptosis in a human ovarian tumor cell line. Biochemical pharmacology *48*, 1265-1272.
783   Luno, V., Lopez-Ubeda, R., Garcia-Vazquez, F.A., Gil, L., and Matas, C. (2013). Boar sperm tyrosine
784   phosphorylation patterns in the presence of oviductal epithelial cells: in vitro, ex vivo, and in vivo
785   models. Reproduction *146*, 315-324.
786   Ma, F., Wu, D., Deng, L., Secrest, P., Zhao, J., Varki, N., Lindheim, S., and Gagneux, P. (2012). Sialidases
787   on mammalian sperm mediate deciduous sialylation during capacitation. Journal of Biological Chemistry
788   *287*, 38073-38079.
789   Ma, X., Pan, Q., Feng, Y., Choudhury, B.P., Ma, Q., Gagneux, P., and Ma, F. (2016). Sialylation facilitates
790   the maturation of mammalian sperm and affects its survival in female uterus. Biology of reproduction
791   *94*, 123, 121-110.

792   Mortimer, D., and Templeton, A. (1982). Sperm transport in the human female reproductive tract in
793   relation to semen analysis characteristics and time of ovulation. Reproduction *64*, 401-408.
794   Muro, Y., Hasuwa, H., Isotani, A., Miyata, H., Yamagata, K., Ikawa, M., Yanagimachi, R., and Okabe, M.
795   (2016). Behavior of Mouse Spermatozoa in the Female Reproductive Tract from Soon after Mating to
796   the Beginning of Fertilization. Biol Reprod *94*, 80.
797   Murray, E., Cho, J.H., Goodwin, D., Ku, T., Swaney, J., Kim, S.-Y., Choi, H., Park, Y.-G., Park, J.-Y., and
798   Hubbert, A. (2015). Simple, scalable proteomic imaging for high-dimensional profiling of intact systems.
799   Cell *163*, 1500-1514.
800   Navarrete, F.A., Garcia-Vazquez, F.A., Alvau, A., Escoffier, J., Krapf, D., Sanchez-Cardenas, C., Salicioni,
801   A.M., Darszon, A., and Visconti, P.E. (2015). Biphasic role of calcium in mouse sperm capacitation
802   signaling pathways. J Cell Physiol *230*, 1758-1769.
803   Neill, J.M., and Olds-Clarke, P. (1987). A computer-assisted assay for mouse sperm hyperactivation
804   demonstrates that bicarbonate but not bovine serum albumin is required. Gamete research *18*, 121-
805   140.
806   Nixon, B., Aitken, R.J., and McLaughlin, E.A. (2007). New insights into the molecular mechanisms of
807   sperm-egg interaction. Cell Mol Life Sci *64*, 1805-1823.
808   Ono, Y., Saido, T.C., and Sorimachi, H. (2016). Calpain research for drug discovery: challenges and
809   potential. Nature Reviews Drug Discovery *15*, 854.
810   Puga Molina, L.C., Luque, G.M., Balestrini, P.A., Marin-Briggiler, C.I., Romarowski, A., and Buffone, M.G.
811   (2018). Molecular Basis of Human Sperm Capacitation. Front Cell Dev Biol *6*, 72.
812   Qi, H., Moran, M.M., Navarro, B., Chong, J.A., Krapivinsky, G., Krapivinsky, L., Kirichok, Y., Ramsey, I.S.,
813   Quill, T.A., and Clapham, D.E. (2007). All four CatSper ion channel proteins are required for male fertility
814   and sperm cell hyperactivated motility. Proc Natl Acad Sci U S A *104*, 1219-1223.
815   Ram, P.A., Cardullo, R.A., and Millette, C.F. (1989). Expression and topographical localization of cell
816   surface fucosyltransferase activity during epididymal sperm maturation in the mouse. Gamete research
817   *22*, 321-332.
818   Ren, D., Navarro, B., Perez, G., Jackson, A.C., Hsu, S., Shi, Q., Tilly, J.L., and Clapham, D.E. (2001). A sperm
819   ion channel required for sperm motility and male fertility. Nature *413*, 603-609.
820   Rottger, S., White, J., Wandall, H.H., Olivo, J.-C., Stark, A., Bennett, E.P., Whitehouse, C., Berger, E.G.,
821   Clausen, H., and Nilsson, T. (1998). Localization of three human polypeptide GalNAc-transferases in HeLa
822   cells suggests initiation of O-linked glycosylation throughout the Golgi apparatus. Journal of Cell Science
823   *111*, 45-60.
824   Sakkas, D., Leppens-Luisier, G., Lucas, H., Chardonnens, D., Campana, A., Franken, D., and Urner, F.
825   (2003). Localization of tyrosine phosphorylated proteins in human sperm and relation to capacitation
826   and zona pellucida binding. Biology of reproduction *68*, 1463-1469.
827   Sakkas, D., Ramalingam, M., Garrido, N., and Barratt, C.L. (2015). Sperm selection in natural conception:
828   what can we learn from Mother Nature to improve assisted reproduction outcomes? Hum Reprod
829   Update *21*, 711-726.
830   Scully, N.F., and Shur, B.D. (1988). Stage-specific increase in cell surface galactosyltransferase activity
831   during spermatogenesis in mice bearing t alleles. Developmental biology *125*, 195-199.
832   Steptoe, P.C., and Edwards, R.G. (1976). Reimplantation of a human embryo with subsequent tubal
833   pregnancy. Lancet *1*, 880-882.
834   Stewart, C.A., and Behringer, R.R. (2012). Mouse oviduct development. In Mouse Development
835   (Springer), pp. 247-262.
836   Stival, C., Ritagliati, C., Xu, X., Gervasi, M.G., Luque, G.M., Baro Graf, C., De la Vega-Beltran, J.L., Torres,
837   N., Darszon, A., Krapf, D*., et al.* (2018). Disruption of protein kinase A localization induces acrosomal
838   exocytosis in capacitated mouse sperm. J Biol Chem *293*, 9435-9447.

839   Suarez, S. (2006). Interactions of spermatozoa with the female reproductive tract: inspiration for
840   assisted reproduction. Reproduction, Fertility and Development *19*, 103-110.
841   Suarez, S.S. (2002). Formation of a reservoir of sperm in the oviduct. Reprod Domest Anim *37*, 140-143.
842   Tateno, H., Krapf, D., Hino, T., Sanchez-Cardenas, C., Darszon, A., Yanagimachi, R., and Visconti, P.E.
843   (2013). Ca2+ ionophore A23187 can make mouse spermatozoa capable of fertilizing in vitro without
844   activation of cAMP-dependent phosphorylation pathways. Proc Natl Acad Sci U S A *110*, 18543-18548.
845   Tonks, N.K. (2005). Redox redux: revisiting PTPs and the control of cell signaling. Cell *121*, 667-670.
846   Tulsiani, D.R. (2003). Glycan modifying enzymes in luminal fluid of rat epididymis: are they involved in
847   altering sperm surface glycoproteins during maturation? Microscopy research and technique *61*, 18-27.
848   Urner, F., Leppens-Luisier, G., and Sakkas, D. (2001). Protein tyrosine phosphorylation in sperm during
849   gamete interaction in the mouse: the influence of glucose. Biology of reproduction *64*, 1350-1357.
850   Visconti, P.E., Bailey, J.L., Moore, G.D., Pan, D., Olds-Clarke, P., and Kopf, G.S. (1995). Capacitation of
851   mouse spermatozoa. I. Correlation between the capacitation state and protein tyrosine
852   phosphorylation. Development *121*, 1129-1137.
853   Visconti, P.E., Ning, X., Fornes, M.W., Alvarez, J.G., Stein, P., Connors, S.A., and Kopf, G.S. (1999).
854   Cholesterol efflux-mediated signal transduction in mammalian sperm: cholesterol release signals an
855   increase in protein tyrosine phosphorylation during mouse sperm capacitation. Dev Biol *214*, 429-443.
856   Vyklicka, L., and Lishko, P.V. (2020). Dissecting the signaling pathways involved in the function of sperm
857   flagellum. Curr Opin Cell Biol *63*, 154-161.
858   Wang, J., and Sauer, M.V. (2006). In vitro fertilization (IVF): a review of 3 decades of clinical innovation
859   and technological advancement. Therapeutics and clinical risk management *2*, 355.
860   Yamaguchi, R., Muro, Y., Isotani, A., Tokuhiro, K., Takumi, K., Adham, I., Ikawa, M., and Okabe, M.
861   (2009). Disruption of ADAM3 impairs the migration of sperm into oviduct in mouse. Biol Reprod *81*, 142-
862   146.
863   Yang, B., Treweek, J.B., Kulkarni, R.P., Deverman, B.E., Chen, C.-K., Lubeck, E., Shah, S., Cai, L., and
864   Gradinaru, V. (2014). Single-cell phenotyping within transparent intact tissue through whole-body
865   clearing. Cell *158*, 945-958.
866   Yousefi, S., Green, D.R., Blaser, K., and Simon, H.-U. (1994). Protein-tyrosine phosphorylation regulates
867   apoptosis in human eosinophils and neutrophils. Proceedings of the National Academy of Sciences *91*,
868   10868-10872.

869
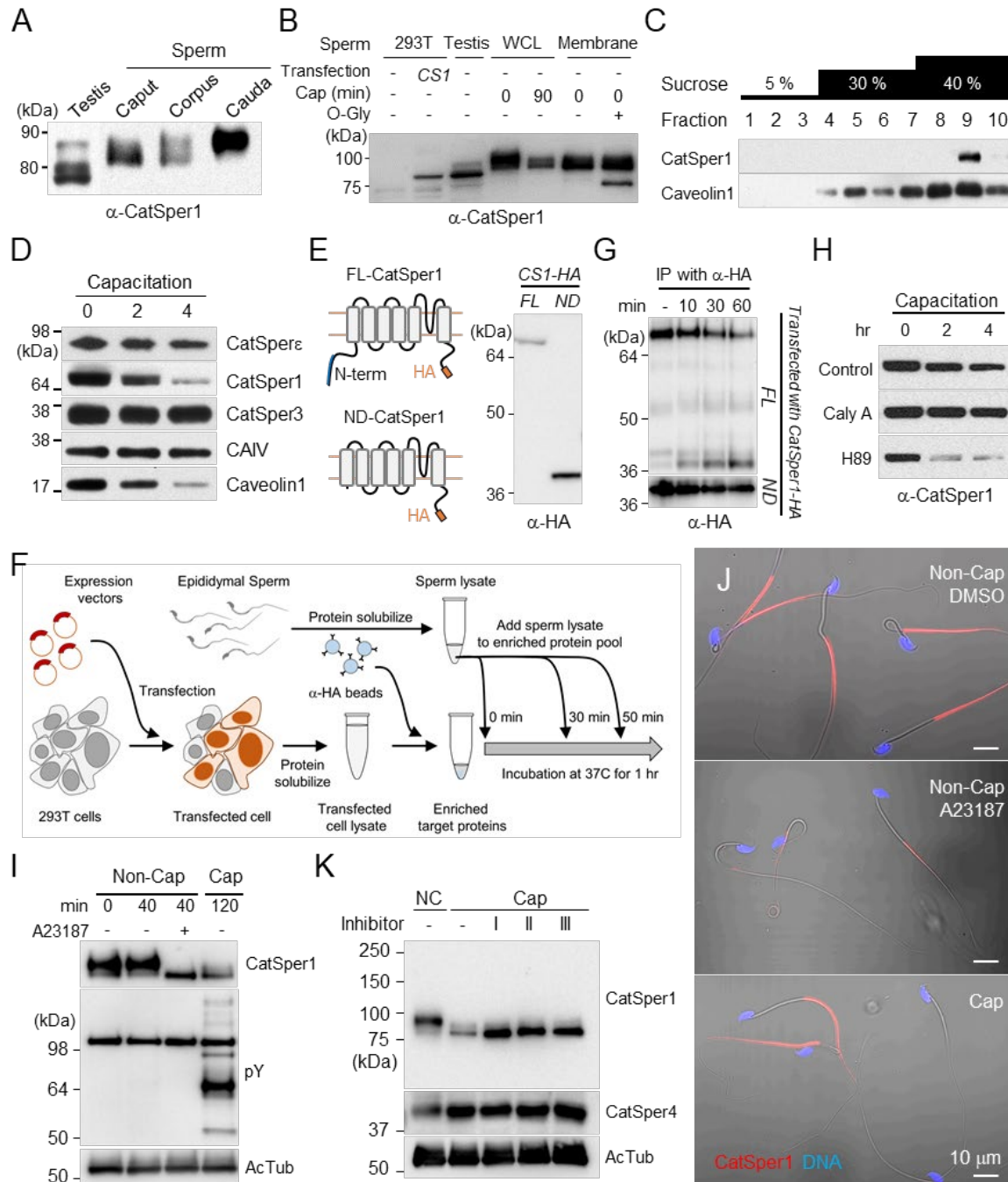
870
871
872 **Figure 1. CatSper1 is specifically processed during *in vitro* capacitation.** (A-B) CatSper1 undergoes
873 post-translational modification during spermiogenesis and epididymal maturation. (A) A gradual decrease
874 in electrophoretic mobility of CatSper1 is observed by Western blot analysis. (B) CatSper1 from sperm
875 membrane fraction are shifted by O-glycosidase (O-Gly). (C) CatSper resides in lipid rafts subdomains of
876 the plasma membrane in mature sperm. Solubilized sperm proteins were fractionized by discontinuous
877 sucrose density gradient (5, 30, and 40%) centrifugation. (D) CatSper1 is degraded during the late stage
878 of capacitation. Protein expression levels of CatSper1 and caveolin-1, but not CatSper3, CatSperε, or
879 carbonic anhydrase 4 (CAIV) are altered by *in vitro* capacitation. (E-G) CatSper1 is cleaved within the N-
880 terminal domain (NTD). (E) A cartoon of full-length (FL, *top*) and N-terminal truncated (ND, *bottom*)

881   recombinant CatSper1 protein expressed in the study (*left*). Both proteins are tagged with HA at their
882   respective C-termini (orange). CatSper1 antibody used in this study is raised against the 1-150 aa region
883   of CatSper1 (blue, Ren et al., 2001). Detection of recombinant FL-CatSper1 and ND-CatSper1 expressed
884   in 293T cells (*right*). (F) A cartoon of the experimental scheme to test NTD truncation of CatSper1. FL-
885   CatSper1 and ND-CatSper1 expressed in 293T cells were solubilized and pulled-down using agarose resin
886   conjugated with HA antibody. The enriched recombinant proteins were incubated with solubilized sperm
887   lysates at 37 °C for 0, 10, 30, and 60 min and subjected to immunoblot. (G) FL-CatSper1 is cleaved at NTD
888   by solubilized sperm lysate. FL-CatSper1 (arrow) decreases while truncated form (arrowhead) increases
889   by incubation with solubilized sperm lysates (*top*). ND-CatSper1 proteins remain largely unchanged under
890   the same conditions (*bottom*). Immunoblotting were performed with HA antibody (E and G). (H)
891   Capacitation-associated CatSper1 degradation is regulated by phosphorylation. CatSper1 degradation is
892   accelerated by PKA inhibition. A PKA inhibitor, H89 (50 μM), enhances capacitation-associated CatSper1
893   degradation. A protein phophatase1 inhibitor, calyculin A (Caly A, 0.1 μM), prevents the CatSper1
894   degradation during sperm capacitation *in vitro*. (I-J) Ca^{2+} influx accelerates CatSper1 degradation. (I)
895   CatSper activation during capacitation and Ca^{2+} ionophore treatment (A23187, 10 μM) facilitates the
896   CatSper1 cleavage. (J) Immunodetection of CatSper1 in the spermatozoa incubated under the conditions
897   used in (I). The extent of CatSper1 degradation is heterogeneous in the capacitated sperm cells (*bottom*)
898   compared with A23187-treated uncapacitated sperm cells (middle). (K) Capacitation-associated CatSper1
899   degradation is blocked by calpain inhibitors (I, II, and III). 20 μM of each calpain inhibitor was treated to
900   sperm during capacitation.
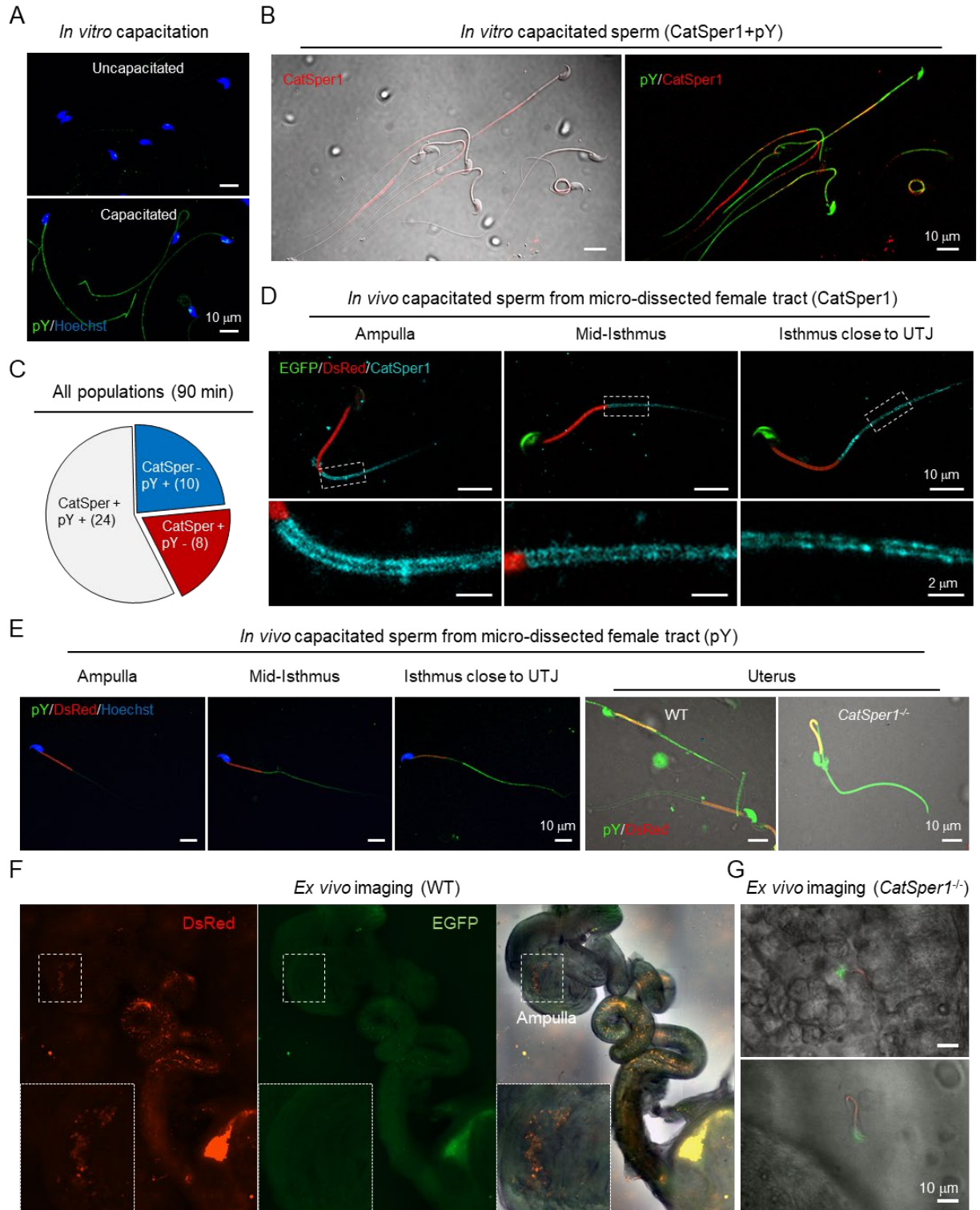
Figure 2. Sperm cells become heterogeneous functionally and molecularly along the female tract.
(A) Immunodetection of pY from *in vitro* capacitated sperm. (B) Sperm cells that maintain intact CatSper1 during *in vitro* capacitation exhibit reduced pY development. An image of CatSper1 (red) is merged with the corresponding DIC image (*left*) or pY image (*right*). (C) A pie chart represents expression patterns of CatSper1 and pY in individual sperm capacitated *in vitro*. Sperm number in each group are indicated in

908   parentheses. *Su9-DsRed;Acr-EGFP* WT and *Su9-DsRed;Acr-EGFP CatSper1$^{-/-}$* mice (Chung et al., 2014)
909   were used for mating. Sperm were capacitated *in vitro* for 90 min (A-B). (D-E) Sperm cells capacitated *in*
910   *vivo* show distinct molecular characteristics along the female tract. The degrees of CatSper1 processing
911   (D) and development of tyrosine phosphorylation (pY) (E) during *in vivo* capacitation were analyzed by
912   immunostaining of the sperm cells at different regions of microdissected female tracts 8h post-coitus. The
913   indicated regions are magnified to show distributions of CatSper1 in sperm cells. Sperm cells that arrived
914   at the ampulla are acrosome reacted and CatSper1 intact (D) and lack pY development (E). Gradual
915   increase of pY is observed in the oviductal sperm located closer to UTJ. Sperm cells that fail to pass UTJ
916   and reside in the uterus show heterogeneous patterns of pY. *CatSper1$^{-/-}$* sperm recovered from the uterus
917   of a mated female show robust elevation of pY. (F-G) WT sperm cells, but not *CatSper1$^{-/-}$* sperm, that arrive
918   at the ampulla are acrosome reacted. *Ex vivo* imaging of female tracts mated with WT (F) and *CatSper1$^{-/-}$*
919   (G) males (8 h post-coitus). (F) WT sperm cells are acrosome-reacted at the ampulla (EGFP-negative,
920   *inset*). (G) A few *CatSper1$^{-/-}$* sperm cells observed at ampulla have intact acrosome (EGFP-positive). Red,
921   DsRed; green, EGFP; Merged, fluorescent images merged with the corresponding DIC image.

922
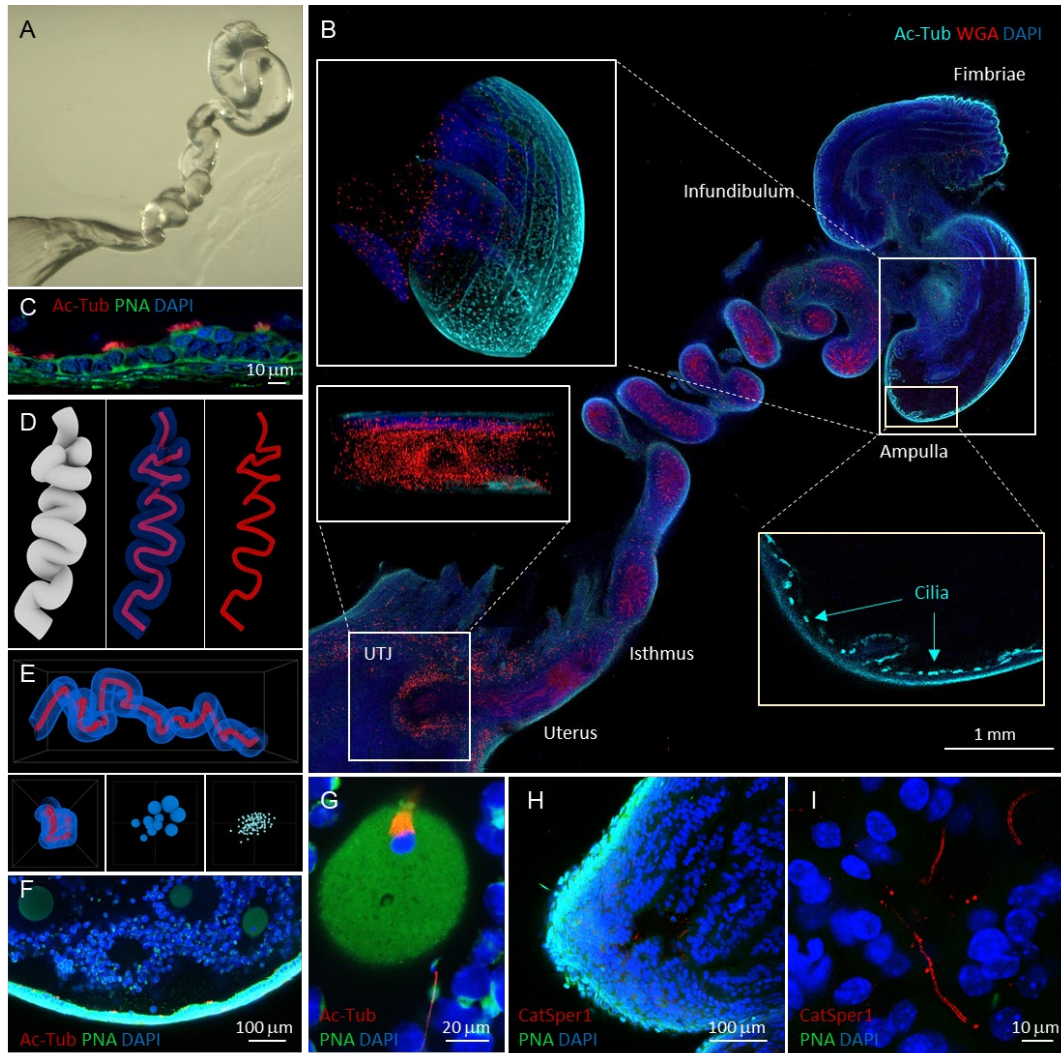
Figure 3. Tissue clearing preserves morphology of female reproductive tract and enables molecular imaging and post-processing of gametes *in situ*. (A) Refractive index-matched cleared mouse female reproductive tract by CLARITY-based tissue clearing. (B) Optical imaging of the cleared female reproductive tract stained by WGA (red), Ac-Tub antibody (cyan) and DAPI (blue), 100x. Insets show cilia stained by Ac-Tub antibody in 2D (*lower right*), a 3D (*upper left*) projection of the ampulla, and a UTJ cross-section (*lower left*). (C) Details of the ampullar epithelium stained by PNA (green), Ac-Tub antibody (red) and DAPI (blue), 400x. (D) 3D digital image reconstruction of the oviduct representing different 3D images rendered for oviductal surface (*left*) and central lumen of oviduct with (*middle) or* without (*right)* oviductal volume information. (E) Morphometric and fluorescent signal quantification analysis of the oviduct showing the morphometric meshwork representation of the 3D volumetric data from the oviduct imaging (*upper*), the corresponding side view (*lower left*) and the non-numerical visual representations of the basic volumetric (*lower middle*) and fluorescent (*lower right*) properties. (F) A fluorescent image showing a closer look of the cleared ampulla with oocytes (oocyte magnified in the panel G on the right-most side), 100x. (G) An oocyte with the meiotic spindle; a sperm cell is approaching the *zona pellucida* directly inside the ampulla, PNA (green), anti-AcTub antibody (red) and DAPI (blue), 630x. (H) A tile-scanned confocal image of epithelium of the cleared ampulla (8h post coitus) stained by anti-CatSper1 antibody (red), PNA (green) and DAPI (blue), 100x. (I) Details of the sperm stained directly inside the ampulla by anti-CatSper1 antibody (red). Two linear CatSper domains are clearly recognizable by confocal imaging. Cell nuclei are stained with DAPI (blue); acrosomes are stained with PNA (green). See also Videos 3-7.

942

943
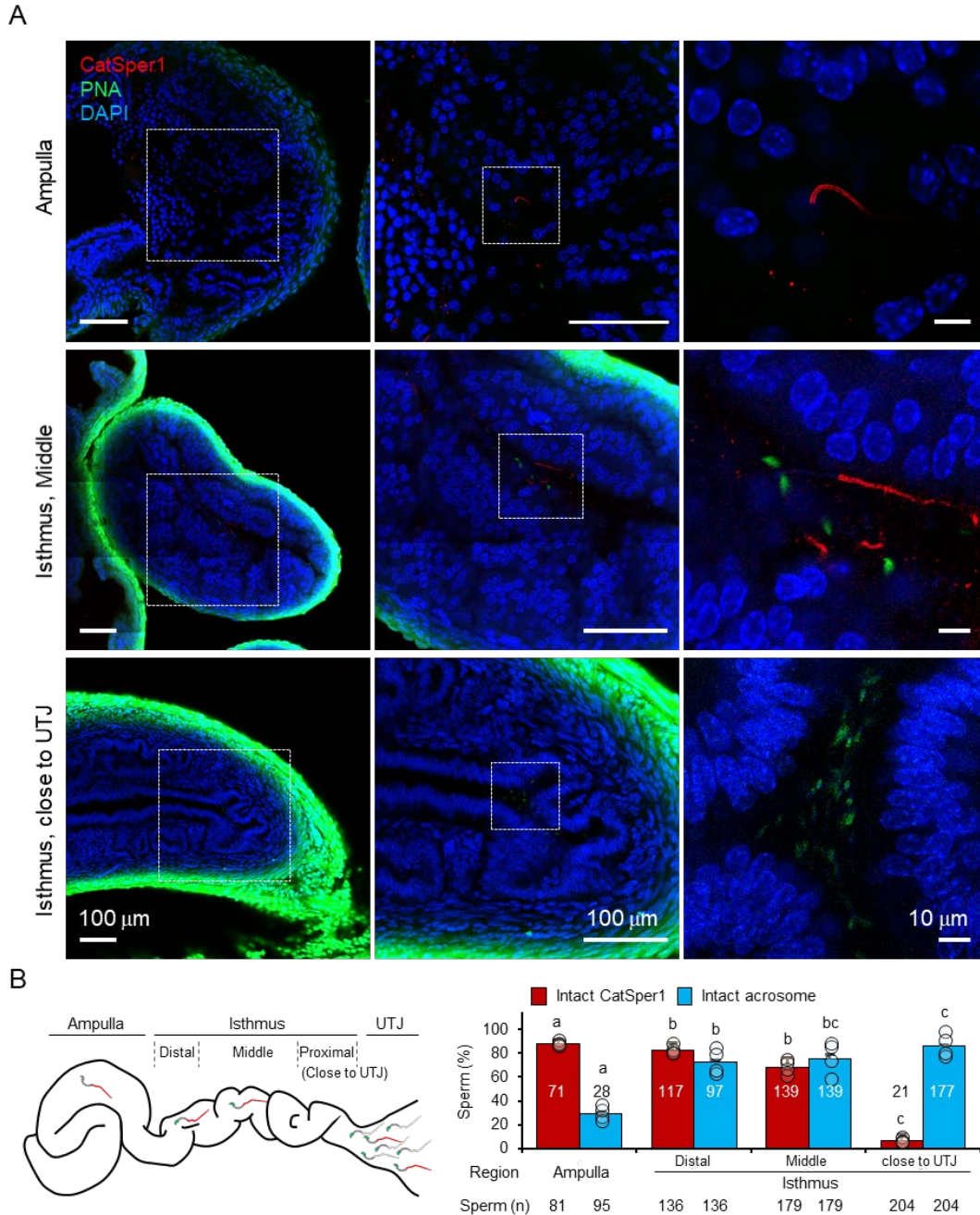
Figure 4. *In situ* molecular imaging of sperm reveals the changes in acrosomal status and CatSper1 fluorescent patterns during capacitation along the female tract. (A) Fluorescent confocal microscope images of acrosome and CatSper1 fluorescent patterns from 3 different regions along the cleared female reproductive tract (Ampulla, *upper*; Middle isthmus, *middle*; Proximal isthmus, *lower*) with different magnifications of the corresponding areas. (B) A cartoon image of the female reproductive tract showing the approximate boundaries between the regions of interest (*left*) used as grouping variable in the subsequent quantification (*right*). The total number of CatSper1-intact sperm (red columns), or acrosome-intact sperm (blue columns), that were counted is shown (bottom). Four independent experiments were performed (n=4). Circles indicate the proportion of sperm cells in each examined site from an independent experiment. Means with different letters indicate significant difference (*P<0.05*) in pairwise comparison between the different regions of female tract. Data is represented to mean ± S.E.M. See also Video 8.
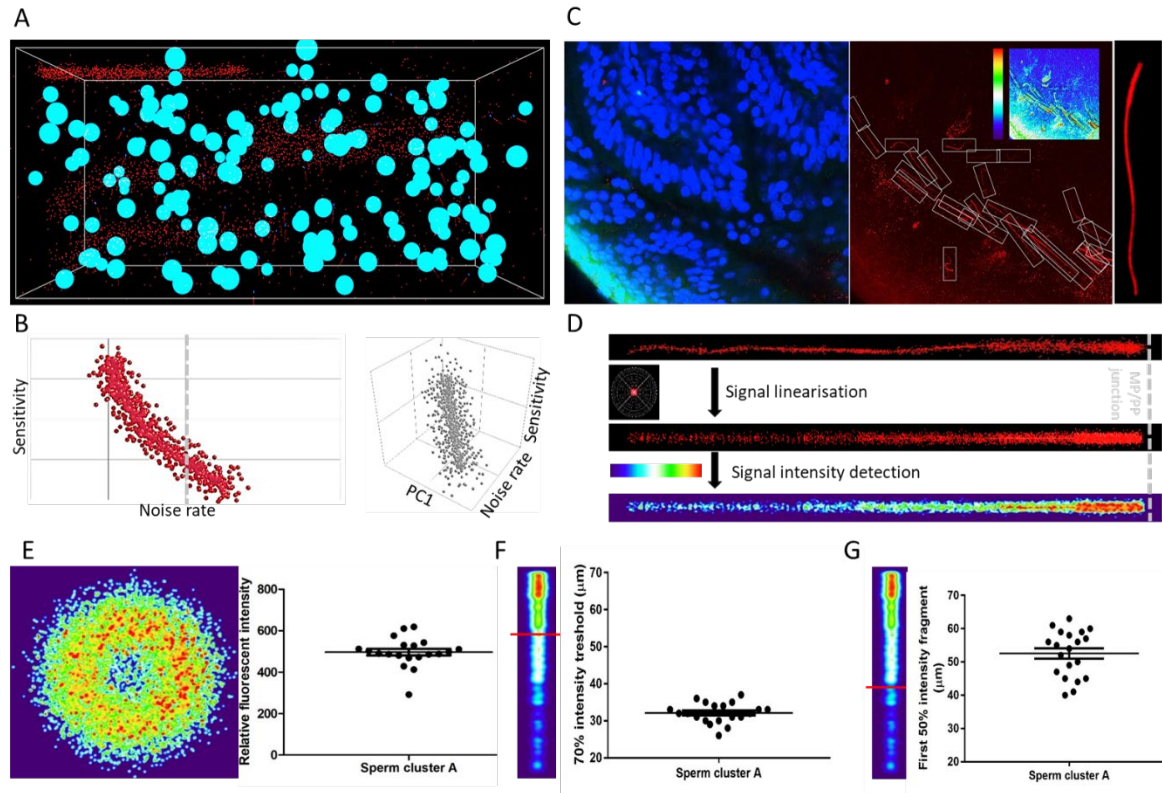
Figure 5. ANN automatically detects fluorescent patterns from 3D volume images of a cleared female reproductive tract, enabling isolation and statistical comparisons of sperm cells. (A) A 3D training environment for ANN emulating sperm cells, somatic nuclei, and noise. (B) Examples of ANN training statistics showing the trend of correlation between the noise rate in the training environment and the sensitivity of ANN (*left*), and a three-dimensional correlation trend between noise rate in the training environment, sensitivity and principal component (PC1) consisting of sperm and nuclei abundancies (*right*). (C) A microscopic focal plane image of the sperm cluster inside the cleared female reproductive tract used for evaluating the ANN performance in real sample (*left*), its superposition in the CatSper1 channel with the individual sperm tails in detection frames with the inset analytical heatmap (*middle*) and the magnification of one of the analytical frames with a CatSper1-positive sperm tail (*right*). (D) Representation of the fluorescent signal in the sperm tail after normalizing individual voxels to signal from the corresponding sperm nucleus (*upper*), after applying linearization and overlay algorithms (*middle*), and heatmap representation of the relative fluorescent intensities among multiple sperm tail (*lower*). (E) Analysis of the relative intensities of the fluorescent signals from sperm located inside the mid-isthmus cleared female reproductive oviduct. The left panel represents the intensity of CatSper1 fluorescent signal in the cross-section of one sperm tail from 20 individual sperm under analysis (middle isthmus). The right panel show the distribution of relative fluorescent intensity of the 20 sperm. (F) Analysis of the continuity of the fluorescent signal along the individual sperm tails; the first fragment of the 70% signal intensity decreases from the midpiece/principal piece interface. (G) The first fragment of the 50% signal intensity decreases from the midpiece/principal piece interface. See also Video 9.

976
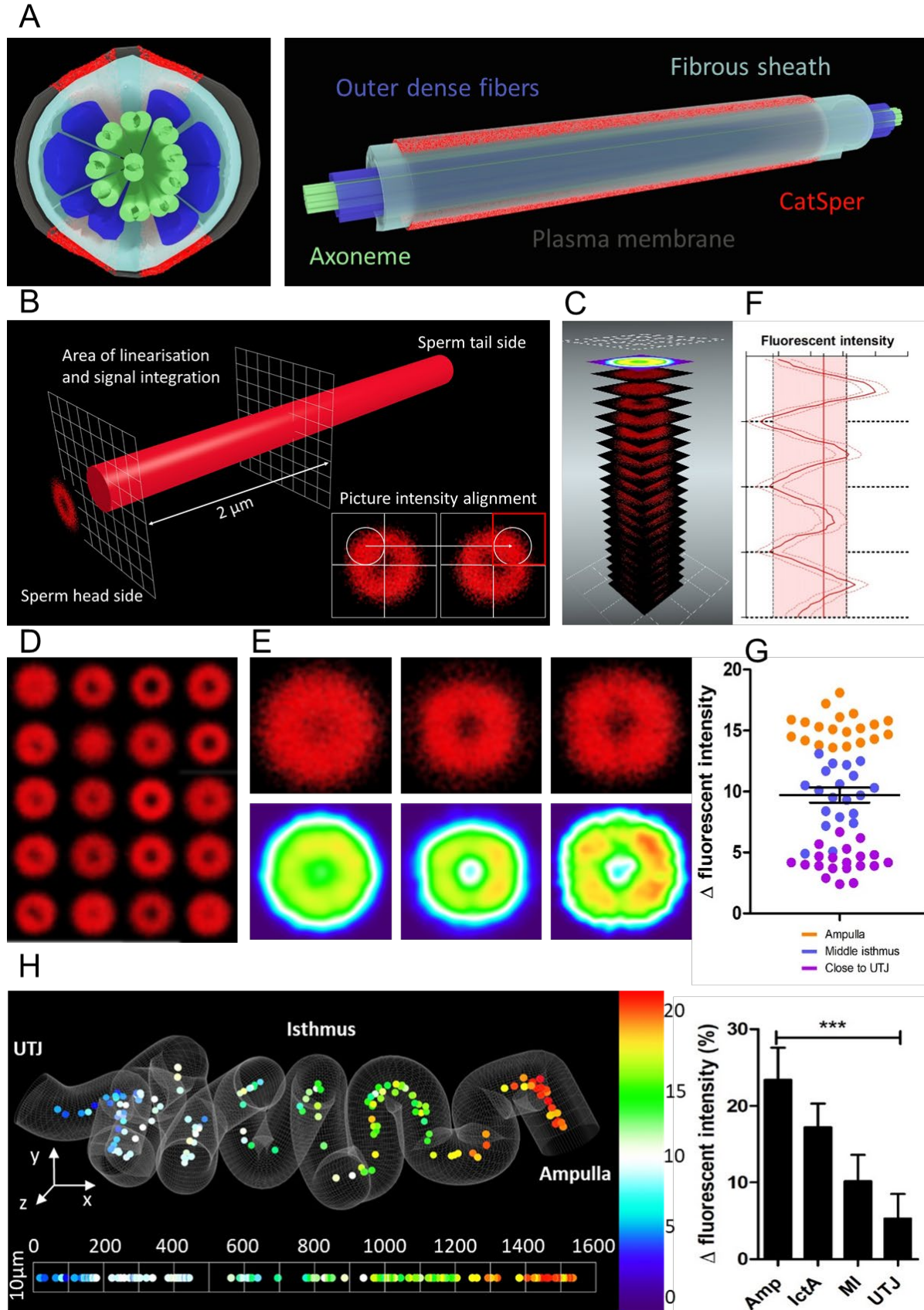
977 **Figure 6. ANN assessment of quadrilateral CatSper nanodomains and Δ fluorescent intensity in**
978 **sperm population along the cleared female tract conforms to findings by other approaches used**
979 **in this study.** (A) 3D perspective schematic views of quadrilateral CatSper nanodomains. A cross-section
980 (*left*). A side view (*right*). (B) A schematic diagram describing the image processing procedure. (C) An
981 illustration of generating ta heatmap from the pre-processed micrographs. (D) 20 processed micrographs
982 of the CatSper1 signal from the sperm cluster from middle isthmus of the cleared oviduct. (E) Processed
983 micrographs (*upper*) and their corresponding heatmaps (*lower*) from 20 spermatozoa from the oviduct
984 close to UTJ (*left*), middle isthmus (*middle*), and ampulla (*right*). (F) An example of fluorescent intensity
985 analysis of processed images showing the 4 peaks corresponding to four CatSper1 quadrilateral domains
986 and calculated averaged Δ value (transversal red line). (G) Analysis of the fluorescent intensity
987 differences (Δ values; red area in panel F) among 3 sperm populations from ampulla, middle isthmus and
988 isthmus close to UTJ. (H) A topological heatmap showing the integrity of the quadrilateral CatSper
989 domain organization represented by Δ values along the morphometrical space of the cleared oviduct (*left*)
990 with the corresponding inferential statistical analysis of the differences of the signal intensities (Δ values,
991 *right*) among four sperm populations (Amp – Ampulla, IctA – isthmus close to ampulla, MI – middle
992 isthmus, UTJ – utero-tubal junction).